Astronomy & Astrophysics manuscript no. planck˙isw˙2015
February 6, 2015

Planck 2015 results. XXI. The integrated Sachs-Wolfe effect

Planck Collaboration: P. A. R. Ade[89], N. Aghanim[62], M. Arnaud[76], M. Ashdown[72,6], J. Aumont[62], C. Baccigalupi[88], A. J. Banday[100,10], R. B. Barreiro[68], N. Bartolo[31,69], E. Battaner[102,103], K. Benabed[63,98], A. Benoît[60], A. Benoit-Lévy[25,63,98], J.-P. Bernard[100,10], M. Bersanelli[34,51], P. Bielewicz[100,10,88], A. Bonaldi[71], L. Bonavera[68], J. R. Bond[9], J. Borrill[15,93], F. R. Bouchet[63,91], M. Bucher[1], C. Burigana[50,32,52], R. C. Butler[50], E. Calabrese[96], J.-F. Cardoso[77,1,63], B. Casaponsa[68], A. Catalano[78,75], A. Challinor[65,72,13], A. Chamballu[76,17,62], H. C. Chiang[28,7], P. R. Christensen[85,38], S. Church[95], D. L. Clements[58], S. Colombi[63,98], L. P. L. Colombo[24,70], C. Combet[78], F. Couchot[73], A. Coulais[75], B. P. Crill[70,12], A. Curto[6,68], F. Cuttaia[50], L. Danese[88], R. D. Davies[71], R. J. Davis[71], P. de Bernardis[33], A. de Rosa[50], G. de Zotti[47,88], J. Delabrouille[1], F.-X. Désert[56], J. M. Diego[68], H. Dole[62,61], S. Donzelli[51], O. Doré[70,12], M. Douspis[62], A. Ducout[63,58], X. Dupac[41], G. Efstathiou[65], F. Elsner[25,63,98], T. A. Enßlin[82], H. K. Eriksen[66], J. Fergusson[13], R. Fernandez-Cobos[68], F. Finelli[50,52], O. Forni[100,10], M. Frailis[49], A. A. Fraisse[28], E. Franceschi[50], A. Frejsel[85], S. Galeotta[49], S. Galli[63], K. Ganga[1], R. T. Génova-Santos[67,39], M. Giard[100,10], Y. Giraud-Héraud[1], E. Gjerløw[66], J. González-Nuevo[68,88], K. M. Górski[70,104], S. Gratton[72,65], A. Gregorio[35,49,55], A. Gruppuso[50], J. E. Gudmundsson[28], F. K. Hansen[66], D. Hanson[83,70,9], D. L. Harrison[65,72], S. Henrot-Versillé[73], C. Hernández-Monteagudo[14,82], D. Herranz[68], S. R. Hildebrandt[70,12], E. Hivon[63,98], M. Hobson[6], W. A. Holmes[70], A. Hornstrup[18], W. Hovest[82], K. M. Huffenberger[26], G. Hurier[62], S. Ilić[100,10,62], A. H. Jaffe[58], T. R. Jaffe[100,10], W. C. Jones[28], M. Juvela[27], E. Keihänen[27], R. Keskitalo[15], T. S. Kisner[80], R. Kneissl[40,8], J. Knoche[82], M. Kunz[19,62,3], H. Kurki-Suonio[27,46], G. Lagache[5,62], A. Lähteenmäki[2,46], J.-M. Lamarre[75], M. Langer[62], A. Lasenby[6,72], M. Lattanzi[32], C. R. Lawrence[70], R. Leonardi[41], J. Lesgourgues[97,87,74], F. Levrier[75], M. Liguori[31,69], P. B. Lilje[66], M. Linden-Vørnle[18], M. López-Caniego[41,68], P. M. Lubin[29], Y.-Z. Ma[23,71], J. F. Macías-Pérez[78], G. Maggio[49], D. Maino[34,51], N. Mandolesi[50,32], A. Mangilli[62,73], A. Marcos-Caballero[68], P. G. Martin[9], E. Martínez-González[68], S. Masi[33], S. Matarrese[31,69,44], P. Mazzotta[36], P. McGehee[59], P. R. Meinhold[29], A. Melchiorri[33,53], L. Mendes[41], A. Mennella[34,51], M. Migliaccio[65,72], S. Mitra[57,70], M.-A. Miville-Deschênes[62,9], A. Moneti[63], L. Montier[100,10], G. Morgante[50], D. Mortlock[58], A. Moss[90], D. Munshi[89], J. A. Murphy[84], P. Naselsky[85,38], F. Nati[28], P. Natoli[32,4,50], C. B. Netterfield[21], H. U. Nørgaard-Nielsen[18], F. Noviello[71], D. Novikov[81], I. Novikov[85,81], C. A. Oxborrow[18], F. Paci[88], L. Pagano[33,53], F. Pajot[62], D. Paoletti[50,52], F. Pasian[49], G. Patanchon[1], O. Perdereau[73], L. Perotto[78], F. Perrotta[88], V. Pettorino[45], F. Piacentini[33], M. Piat[1], E. Pierpaoli[24], D. Pietrobon[70], S. Plaszczynski[73], E. Pointecouteau[100,10], G. Polenta[4,48], L. Popa[64], G. W. Pratt[76], G. Prézeau[12,70], S. Prunet[63,98], J.-L. Puget[62], J. P. Rachen[22,82], W. T. Reach[101], R. Rebolo[67,16,39], M. Reinecke[82], M. Remazeilles[71,62,1], C. Renault[78], A. Renzi[37,54], I. Ristorcelli[100,10], G. Rocha[70,12], C. Rosset[1], M. Rossetti[34,51], G. Roudier[1,75,70], J. A. Rubiño-Martín[67,39], B. Rusholme[59], M. Sandri[50], D. Santos[78], M. Savelainen[27,46], G. Savini[86], B. M. Schaefer[99], D. Scott[23], M. D. Seiffert[70,12], E. P. S. Shellard[13], L. D. Spencer[89], V. Stolyarov[6,72,94], R. Stompor[1], R. Sudiwala[89], R. Sunyaev[82,92], D. Sutton[65,72], A.-S. Suur-Uski[27,46], J.-F. Sygnet[63], J. A. Tauber[42], L. Terenzi[43,50], L. Toffolatti[20,68,50], M. Tomasi[34,51], M. Tristram[73], M. Tucci[19], J. Tuovinen[11], L. Valenziano[50], J. Valiviita[27,46], B. Van Tent[79], P. Vielva[68*], F. Villa[50], L. A. Wade[70], B. D. Wandelt[63,98,30], I. K. Wehus[70], D. Yvon[17], A. Zacchei[49], and A. Zonca[29]

(Affiliations can be found after the references)

Preprint online version: February 6, 2015

ABSTRACT

This paper presents a study of the integrated Sachs-Wolfe (ISW) effect from the *Planck* 2015 temperature and polarization data release. The secondary cosmic microwave background (CMB) anisotropy caused by the large-scale time-evolving gravitational potential is probed from different perspectives. The CMB is cross-correlated with different large-scale structure (LSS) tracers: radio sources from the NVSS catalogue, galaxies from the optical SDSS and the infrared WISE surveys, and the *Planck* 2015 convergence lensing map. The joint cross-correlation of the CMB with the tracers yields a detection at $4\,\sigma$, where most of the signal-to-noise is due to the *Planck* lensing and the NVSS radio catalogue. In fact, the ISW effect is detected only from the *Planck* data (through the ISW-lensing bispectrum) at $\approx 3\,\sigma$, which is similar to the detection level achieved by combining the cross-correlation signal coming from all the galaxy catalogues mentioned above. We study the ability of the ISW effect to place constraints on the dark-energy parameters; in particular, we show that Ω_Λ is detected at more than $3\,\sigma$. This cross-correlation analysis is performed only with the *Planck* temperature data, since the polarization scales available in the 2015 release do not permit significant improvement of the CMB-LSS cross-correlation detectability. Nevertheless, the *Planck* polarization data is used to study the anomalously large ISW signal previously reported through the aperture photometry on stacked CMB features at the locations of known superclusters and supervoids, which is in conflict with ΛCDM expectations. We find that the current *Planck* polarization data do not reject that this signal could be caused by the ISW effect. In addition, the stacking of the *Planck* lensing map on the superstructures' locations exhibits a positive cross-correlation with these large-scale structures. Finally, we have improved our previous reconstruction of the ISW temperature fluctuations by combining the information encoded in all the previously mentioned LSS tracers. In particular, we construct a map of the ISW secondary anisotropies and the corresponding uncertainties map, obtained from simulations. We also explore the reconstruction of the ISW anisotropies caused by the large-scale structure traced by the 2MASS Photometric redshift survey (2MPZ), by directly inverting the density field into the gravitational potential field.

Key words. Cosmology: observations – cosmic microwave background – large-scale structure of the Universe – dark engery – Galaxies: clusters: general – Methods: data analysis

1. Introduction

This paper, one of a set associated with the 2015 release of data from the *Planck*[1] mission, describes the detection and characterization of the integrated Sachs-Wolfe (ISW) effect using external (galaxy-survey catalogues) and internal (*Planck* lensing map) large-scale tracers. The 2015 *Planck* data release offers polarization information on the cosmic microwave background (CMB) for angular scales samller than 5°. Whenever possible, this polarization information is used to improve our characterization of the ISW signal.

The ISW effect (Sachs & Wolfe 1967; Rees & Sciama 1968; Martinez-Gonzalez et al. 1990; Sugiyama 1995) is a secondary anisotropy in the CMB which is caused by gravitational interaction of CMB photons with the growing cosmic large-scale structure (LSS):

$$\Theta = \frac{\Delta T}{T_{\rm CMB}} = -\frac{2}{c^3}\int_0^{\chi_{\rm CMB}} {\rm d}\chi \frac{\partial \Phi}{\partial \chi}. \quad (1)$$

Here, the fractional temperature perturbation Θ is given as a line-of-sight-integral over the time-evolving potentials Φ in the LSS. The integral is expressed in terms of comoving distance χ, which is related to the scale factor a according to ${\rm d}a/{\rm d}\chi = a^2 H(a)/c$ with the Hubble function $H(a)$ and the speed of light c. The integration is extended to the surface of last scattering $\chi_{CMB} \simeq 10$ Gpc$/h$ corresponding to a redshift of $z \simeq 1100$ in a ΛCDM cosmology.

The ISW effect measures the rate of growth of gravitational potentials relative to universes with matter up to the critical density by frequency shifts in the photon distribution. It is measured in cross-correlation with a tracer of the LSS such as a galaxy catalogue or a reconstructed weak gravitational lensing map in order to distinguish it from primary CMB anisotropies, because gravitational interaction conserves the Planckian shape of the photon spectrum. The ISW effect is generated at late times when the growth of structure is influenced by a cosmological constant, dark energy (Crittenden & Turok 1996), modified gravity (Hu 2002), or spatial curvature (Kamionkowski 1996).

The most direct way for detecting the ISW effect is the determination of the cross-correlation or the cross-angular power spectrum between the CMB temperature and the density of tracer objects such as galaxies. In this way, the first detection was reported by Boughn & Crittenden (2004) which was subsequently refined by many groups on the basis of *WMAP* data, yielding values for the detection significance in excess of 4σ (e.g., Fosalba et al. 2003; Nolta et al. 2004; Corasaniti et al. 2005; Padmanabhan et al. 2005; Vielva et al. 2006; Giannantonio et al. 2006; Cabré et al. 2007; Rassat et al. 2007; McEwen et al. 2007; Giannantonio et al. 2012). Corresponding constraints on cosmological parameters were derived for standard cosmologies with a cosmological constant and for dark energy cosmologies (e.g., Pietrobon et al. 2006; McEwen et al. 2007; Vielva et al. 2006; Giannantonio 2008; Ho et al. 2008; Xia et al. 2009) and on the other hand for models with modified gravity (e.g., Zhao et al. 2010). A Bayesian ISW detection method, which estimates the ISW amplitude conditionally to the observed LSS, can be expected to provide 10% better signal-to-noise ratio compared to a direct CMB-LSS cross-correlation study (Frommert et al. 2008), as used traditionally and in this article for its lower computational complexity.

In fact, using the ISW signal alone (but fixing the remaining cosmological parameters) the dark energy density parameter Ω_Λ was estimated to be ≈ 0.75 with an error of about 20% (e.g., Nolta et al. 2004; Vielva et al. 2006; Giannantonio et al. 2006), the dark energy equation of state parameter was found to be close to $w = -1$ (e.g., Vielva et al. 2006; Giannantonio et al. 2006; Ho et al. 2008) and tests on spatial flatness yielded upper limits of a few percent for Ω_K (e.g., Ho et al. 2008; Li & Xia 2010), thus confirming the concordance cosmological model.

The presence of systematics at large angular scales in LSS surveys and their possible impact on ISW studies was first flagged in Hernández-Monteagudo (2010) and formally addressed in Giannantonio et al. (2012); Hernández-Monteagudo et al. (2013). The ISW analysis with the *Planck* data release in 2013 (Planck Collaboration XIX 2014) was consistent with *WMAP* results using the NVSS radio catalogue and catalogues of tracer objects derived with optical SDSS data, while lowering the claimed detection levels to significantly smaller numbers (from $> 4\,\sigma$ down to $2.5\,\sigma$). In addition, a non-zero correlation between the reconstructed CMB-lensing map as a LSS tracer and the microwave background was reported for the first time, using the non-vanishing bispectrum of the CMB anisotropies on the relevant scales. The strength of this correlation was measured to be $3\,\sigma$, and provides further evidence for a late-time accelerated expansion of the Universe, as theoretically shown by Hu & Okamoto (2002); Okamoto & Hu (2003).

An alternative method for detecting the ISW effect is the stacking of CMB fields at the position of known superstructures: if the ISW effect is associated with regions of large density, it should be possible to reduce the noise due to primary, uncorrelated CMB anisotropies by superposition and to reach a reduction inversely proportional to the square root of stacked fields. Detections using this method range between $2\,\sigma$ and $4\,\sigma$ based on *WMAP* data (e.g., Granett et al. 2008a; Pápai et al. 2010) and on *Planck* data (Planck Collaboration XIX 2014).

A third application of the ISW effect is the reconstruction of a large-scale map of projected gravitational potentials (Barreiro et al. 2008): using the correlation between temperature anisotropies and a map of the tracer density, it is possible to estimate these secondary temperature anisotropies.

The purpose of this paper is the measurement of the ISW effect with the full *Planck* 2015 data set and to establish the corresponding constraints on cosmological parameters. In principle, including polarization data allows to reduce the error bars in estimating cross-angular power spectra (Frommert & Enßlin 2009), and it provides a separation of the temperature anisotropies into those correlated and uncorrelated with polarization, by which the secondary nature of the ISW effect can be better investigated. Furthermore, the reconstruction of the weak lensing potential is improved, and a better template for cross-correlation is provided. However, as mentioned above, the current polarization information provided in the CMB maps of the 2015 *Planck* data release is limited to angular scales smaller than 5° (more precisely, only multipoles $\ell \geq 20$ are kept, with a cosine transition between $20 < \ell < 40$). This limits the amount of information on the ISW effect that can be obtained from the polarization data, since this secondary anisotropy is mostly significant on the largest angular scales. Therefore, in this paper, polarization is not used for the CMB cross-correlation with LSS tracers, although it is con-

* Corresponding author: P. Vielva vielva@ifca.unican.es

[1] *Planck* (http://www.esa.int/Planck) is a project of the European Space Agency (ESA) with instruments provided by two scientific consortia funded by ESA member states and led by Principal Investigators from France and Italy, telescope reflectors provided through a collaboration between ESA and a scientific consortium led and funded by Denmark, and additional contributions from NASA (USA).

sidered in the analysis of the CMB anisotropies stacked on the position of known superstructures.

The paper is organized as follows: in Sect. 2 we present the data used in this work (both for the CMB and the LSS tracers). The cross-correlations of these tracers are investigated in Sect. 3. In Sect. 4 we present the results of the stacking analysis using temperature and polarization data. The recovery of the ISW anisotropies map is described in Sect. 5. Finally, we discuss our main results and their cosmological implications in Sect. 6.

2. Data sets

In this section we describe the data sets and the simulations used along the paper. In Sect. 2.1 we describe the CMB related data (temperature and polarization anisotropies), whereas the LSS data sets are given in Sect. 2.2: galaxies, clusters and voids catalogues from redshift and photometric surveys, and the *Planck* lensing map. In Sect. 2.3 we explain the specific simulations performed to study the CMB-LSS cross-correlation.

2.1. CMB data

There are four major *Planck* foreground-cleaned CMB temperature and polarization maps, namely, the `COMMANDER`, `NILC`, `SEVEM`, and `SMICA` maps, named after their respectively generating component separation methods (see Planck Collaboration IX 2015, for details). All these maps are used here in comparison in order to test the robustness of our results. Together with the common Q and U Stokes' parameter polarization maps, the *Planck* 2015 data release also provides E-mode maps based on the four component separation methods. In addition, the `SEVEM` method also provides foreground-cleaned CMB maps at specific frequencies, in temperature at 100, 143 and 217 GHz, and in polarization at 70, 100 and 143 GHz.

The *Planck* 2015 CMB maps are provided at different resolutions (Planck Collaboration IX 2015). In this paper we consider two different of them, depending on the application. First, maps with a `HEALPix` (Górski et al. 2005) resolution parameter $N_{\rm side}$= 64 (FWHM = 160 arcmin) are adopted for studying the CMB-LSS cross-correlation (Sect. 3) and for recovering the ISW anisotropies (Sect. 5). Second, $N_{\rm side}$= 512 (FWHM = 20 arcmin) maps are used to study the ISW effect through the stacking of CMB maps on the positions of known superstructures (Sect. 4). Each resolution has an associated set of masks, one for temperature (called UT78, $f_{\rm sky}$ = 74% at $N_{\rm side}$= 512), another for Q and U Stokes parameters (called UPB77, $f_{\rm sky}$ = 76% at $N_{\rm side}$= 512), and a final one for the E-mode ($f_{\rm sky}$ = 45% at $N_{\rm side}$= 512). The $f_{\rm sky}$ parameter indicates the fraction of the sky that is retained after masking.

In addition, there are 1,000 simulations associated to each delivered map, which allow us to characterize the instrumental properties of *Planck* CMB maps. In the context of this work, these simulations are used for the stacking analyses in Sect. 4. The other ISW studies require specific coherent simulations between the CMB and the LSS tracers. These simulations are described in Sect. 2.3.

As mentioned in the Introduction, the polarized CMB maps of the 2015 release have been high-pass filtered (see Planck Collaboration VII 2015; Planck Collaboration IX 2015, for details). In particular, all the multipoles with $\ell \geq 20$ were cut, and a cosine transition between $20 < \ell < 40$ was imposed. Obviously, this high-pass filtering limits very much the usefulness of the polarization information for the ISW analyses. More precisely, the expected 10% increase of the ISW detection significance by exploiting polarization information in the CMB-LSS cross-correlation (Frommert & Enßlin 2009) depends, unfortunately, mainly on the filtered out scales. Nevertheless, some of the information kept at smaller scales may still be useful for particular analyses as the stacking of the CMB anisotropies on the position of known superstructures.

The primary CMB temperature anisotropies act as a noise for the measurement of secondary CMB anisotropies by increasing its cosmic variance, like the ISW effect, which does not produce a notable E-mode polarization. Hence, polarization data permits us to identify the part of the primary temperature anisotropies, which is correlated with the E-mode polarization, and to remove it from the maps. The resulting CMB temperature map, partly cleaned form primary anisotropies, provides up to a 16% better signal-to-noise ratio for secondary fluctuations (Frommert & Enßlin 2009). To this end, we separate the temperature map in two components: an E-correlated (T_{E-c}) and an E-uncorrelated (T_{E-u}) part. Following the approach of Frommert & Enßlin (2009), we have produced these maps from the delivered CMB inputs described above. An estimation of the E-correlated temperature anisotropies (T_{E-c}) is given, in terms of its spherical harmonic coefficients $a_{\ell m}^{T_{E-c}}$, by

$$a_{\ell m}^{T_{E-c}} = a_{\ell m}^{E} w_\ell, \tag{2}$$

where the filter w_ℓ is defined by the TE and the EE angular power spectra:

$$w_\ell = \frac{C_\ell^{TE} + F_\ell^{TE}}{C_\ell^{EE} + F_\ell^{EE} + N_\ell^{EE}}, \tag{3}$$

with C_ℓ, F_ℓ, and N_ℓ representing the angular power spectra of the CMB, residual foregrounds, and noise, respectively. Hence, the T_{E-c} map is given by:

$$T_{E-c}(\mathbf{n}) = \sum_{\ell=0}^{\ell_{\rm max}} \sum_{m=-\ell}^{\ell} a_{\ell m}^{T_{E-c}} \mathrm{Y}(\mathbf{n}), \tag{4}$$

with $\mathrm{Y}(\mathbf{n})$ the spherical harmonic functions: the T_{E-u} map is build by subtraction: $T_{E-u}(\mathbf{n}) = T(\mathbf{n}) - T_{E-c}(\mathbf{n})$. The above procedure is performed by applying an apodized version of the corresponding masks. In Fig. 1 we show the T, T_{E-c}, and T_{E-u} maps for `SEVEM`. In practice, the determination of the filter w_ℓ is not straightforward: although the CMB and noise contributions can be obtained directly from the *Planck* best-fit cosmological model (Planck Collaboration XIII 2015) and the FFP8 simulations (Planck Collaboration XII 2015; Planck Collaboration IX 2015), information about the residual foregrounds (F_ℓ) present in the CMB temperature and polarization is also needed. We verified that the expected CMB and noise power spectra account well for the observed TE and the EE angular power spectra at $\ell < 200$. Although the foreground spectra are not fully known, their impact is minor on these scales due to the large mask imposed to the E-mode map and the high-pass filtering applied to the polarization data. At smaller angular scales some foreground residuals exist.

An alternative way to construct such a filter to reduce primary anisotropies is to extract the relevant correlation functions directly from the data. In particular, we have constructed filters w_ℓ by a smooth fit of the filter constructed as the ratio of the TE and the EE angular power spectra of the different CMB component separation maps. The procedure followed to build the filter distinguishes between high and low-ℓ regimes.

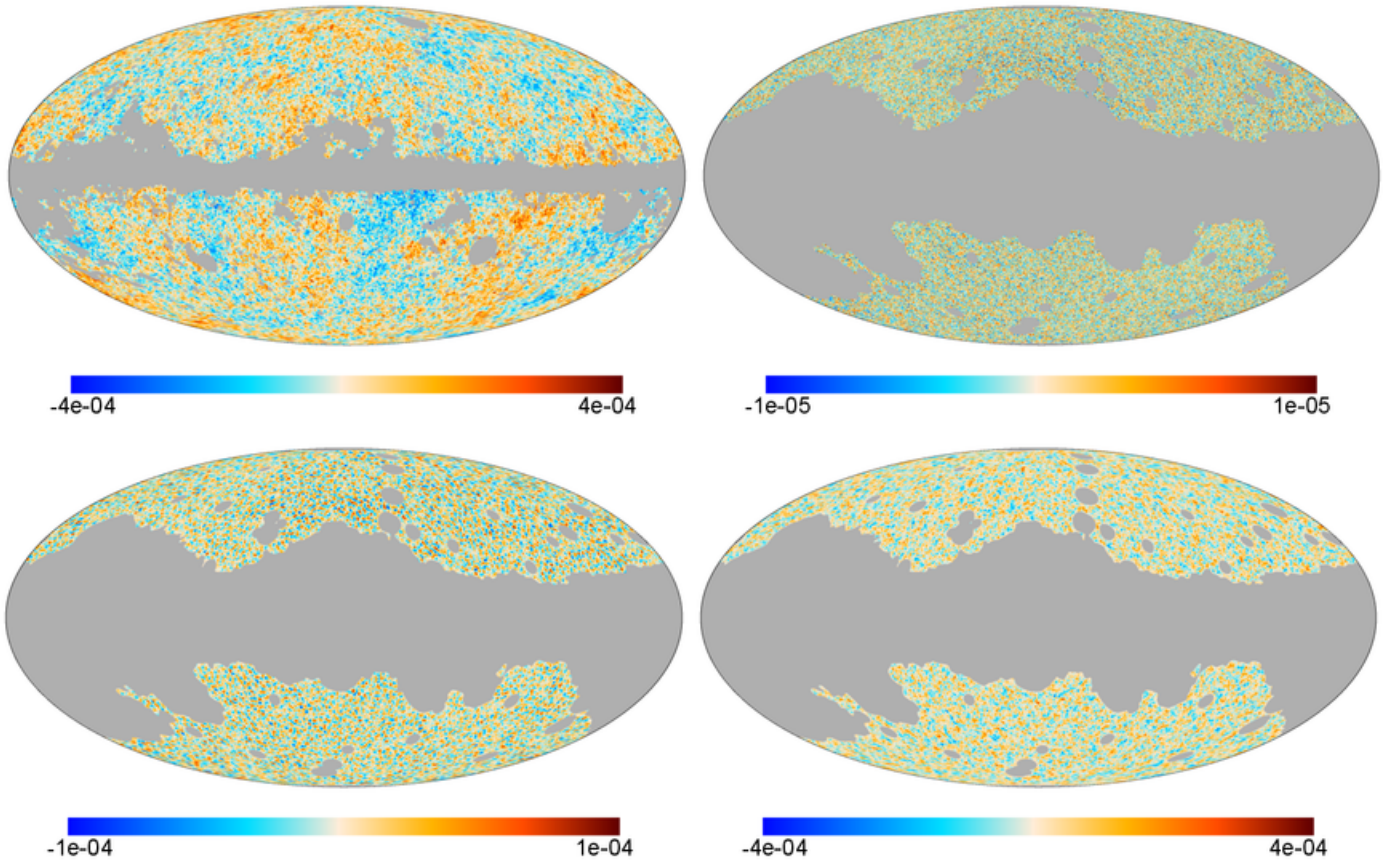

Fig. 1. *Planck* CMB temperature and polarization anisotropies as provided by the SEVEM component separation method at a resolution of $N_{\rm side}$=512. From left to right and from top to bottom, the panels show the maps of temperature,the E-mode, and the E-correlated (T_{E-c}) and E-uncorrelated (T_{E-u}) temperature maps. Units are in Kelvin.

For small scales ($\ell > 200$), we compute the ratio of the C_ℓ^{TE} and C_ℓ^{EE} obtained from the data using an apodized mask, which is afterwards smoothed following the Savitzky-Golay procedure (Savitzky & Golay 1964). In the low-ℓ regime ($\ell < 200$) the filter is constructed using the average value obtained from 1,000 simulations of CMB plus noise using the same apodized mask. The resulting filters (solid lines) are shown in Fig. 2; for comparison, the corresponding theoretical filters computed only from the instrumental properties and the *Planck* fiducial angular power spectra are also plotted (dashed lines).

2.2. LSS tracers

As mentioned in the Introduction, tracers of the gravitational potential of the LSS are required to extract the secondary ISW anisotropies from the dominant primary CMB anisotropies. These tracers are used to perform the CMB-LSS cross-correlation, but also for studying the ISW effect through the stacking of the CMB anisotropies on the position of known superstructures (as clusters or voids), and for producing a map of the ISW anisotropies.

We have included three additional galaxy catalogues with respect to to the ones used in Planck Collaboration XIX (2014) [which were the radio NVSS catalogue and the optical luminous galaxies (SDSS-CMASS/LOWZ) as well as the main photometric galaxy sample (SDSS-MphG) catalogues from the *Sloan Digital Sky Survey* (SDSS)]. These additional catalogues consist of star forming galaxies (WISE-GAL), of AGNs (WISE-AGN),

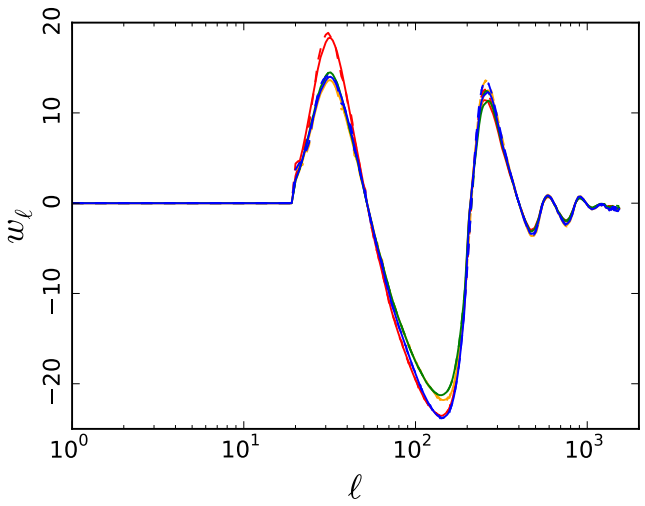

Fig. 2. Filter used to construct the T_{E-c} correlated maps for all component separation methods: COMMANDER in red, NILC in orange, SEVEM in green, and SMICA in blue. The solid lines are obtained directly from the data, whereas the dashed ones represent the theoretical shape of the filters, only considering the instrumental noise characteristics of the data and the fiducial *Planck* angular power spectra.

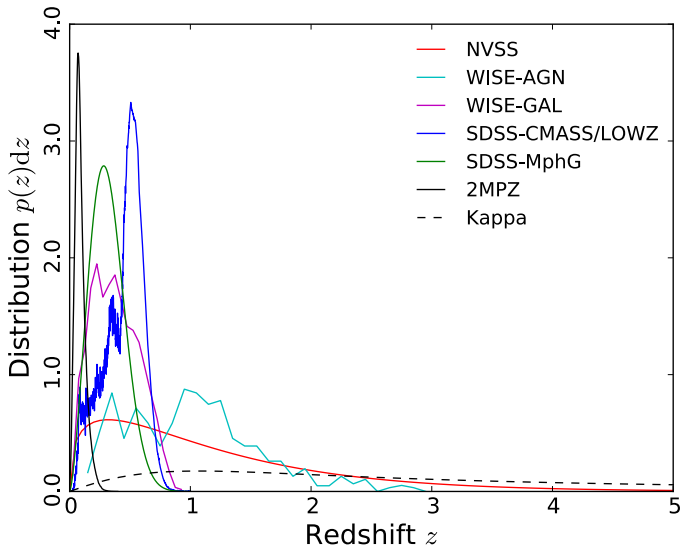

Fig. 3. Redshift distributions of the different surveys used as LSS tracers. To facilitate comparison, the distributions of the external tracers have been normalized to unity (and multiplied by a factor 10 for the 2MPZ catalogues). For completeness, we also include the contribution of the gravitational potential to the lensing convergence map, as a function of redshift (without any additional normalization).

both sets taken from the catalogue of extragalactic sources detected by the *Wide-Field Infrared Survey Explorer* (WISE, see Wright et al. 2010), and of photometric redshifts (2MPZ) obtained from the *Two Micron All Sky Survey* Extended Source Catalogue (2MASS-XSC), WISE and SuperCOSMOS data sets. This last catalogue is only used to build an estimation of the ISW anisotropies based on a reconstruction of the gravitational potential from the 3D distribution of the galaxies (see Sect. 5). More over, we also cross-correlate the *Planck* lensing map as a LSS tracer with the CMB. In particular, we use the lensing convergence map (Kappa) obtained in Planck Collaboration XV (2015).

The redshift distributions of these catalogues are shown in Fig. 3. Note that Kappa, NVSS, and WISE-AGN offer the widest redshift coverage. Some basic properties of the used galaxy catalogues (NVSS, WISE-AGN, WISE-GAL, SDSS-CMASS/LOWZ, SDSS-MphG, and 2MPZ) are summarized in Table 1.

For a better visualization, Wiener-filtered versions of the all-sky density projection of the external catalogues, as well as the *Planck* Kappa map, are shown in Fig. 4, which are constructed from the theoretical power spectra obtained as described in Sect. 2.3. The corresponding angular power spectra are given in Fig. 5. We show the auto- and the cross- angular spectra for all the LSS tracers: dashed lines and points correspond to the theoretical model and the data measurements, respectively (red for auto-spectra, and blue for cross-spectra); grey areas represent their 1 σ sampling uncertainties due to cosmic variance. All these spectra have been corrected from the mask coupling following the `MASTER` approach (Hivon et al. 2002). Notice that the *Planck* lensing convergence map (Kappa) only contains information for multipoles $\ell > 8$ (see Planck Collaboration XV 2015, for details). The two maps based on the WISE catalogues (WISE-AGN and WISE-GAL) exhibit some extra signal at the largest scales (clearly seen not only in the auto-spectra, but also in their cross-power spectra with other surveys). We identify this with some systematics present in these catalogues and, therefore, as a baseline, we only consider multipoles $\ell > 9$ for these two surveys. This cut implies only a minor loss of the ISW signal, while permitting a more robust determination of it. The three maps (Kappa, WISE-AGN, and WISE-GAL) shown in Fig. 4 do not include the cut multipoles.

Besides the galaxy surveys described above, we also use superstructures catalogues to study the ISW effect through the stacking of the CMB anisotropies on the position of clusters and voids. We concentrate on the superclusters and voids catalogue of Granett et al. (2008b), obtained from SDSS (GR0808), since, as shown in Planck Collaboration XIX (2014), its reported strong signal would be a challenge for the standard ΛCDM cosmology if it is solely caused by the ISW effect.

Below we provide a description of all these LSS tracers. For those catalogues already used in our previous publication (NVSS, SDSS-CMASS/LOWZ, SDSS-MphG, and GR0808) only a summary is provided. A more detailed description can be found in Planck Collaboration XIX (2014).

2.2.1. The NVSS radio-galaxies catalogue

The luminous active galactic nuclei (hereafter AGN) are very powerful radio sources, which can be seen also at high redshifts. These sources are able to trace the cosmic density field for both the redshift evolution and the spatial distribution. Therefore the sources can probe the spatial distribution of large-scale potential wells that contribute to generate the ISW effect during the dark energy era.

The sources we use in this paper are the same samples we use in Planck Collaboration XIX (2014), i.e. the NRAO Vary-Large-Array (VLA) Sky Survey (Condon et al. 1998). This NVSS survey was conducted by using VLA at 1.4 GHz, and covers up to an equatorial latitude of $b_{\rm E} = -40°$, with an average noise level of 0.45 mJy beam^{-1}. Thus there are roughly 1.4×10^6 sources above a flux threshold of 2.5 mJy. Figure 4 (top-left panel) shows the all-sky density projection for the NVSS galaxies, where the grey area indicates regions not observed or disregarded by the surveys. Figure 5 includes a sub-plot to show the angular power spectra (blue points) of the NVSS survey.

For the galaxy bias, we use the Gaussian bias evolution model of Xia et al. (2011), i.e., the bias of the survey is given by a mass-weighted integral,

$$b(z) = \frac{\int_{M_{\rm min}}^{\infty} \mathrm{d}M\; b(M,z)\; M\; n(M,z)}{\int_{M_{\rm min}}^{\infty} \mathrm{d}M\; M\; n(M,z)} \,. \qquad (5)$$

where $n(M,z)$ is the halo mass function for which we adopt the Sheth-Tormen (Sheth & Tormen 1999) mass function and $b(M,z)$ is the bias of halos with comoving mass M. This bias (as a function of redshift) can be approximated to a second order polynomial, as given in Table 1. In addition, the redshift distribution is parametrized by:

$$\frac{\mathrm{d}n}{\mathrm{d}z} = n_0 \left(\frac{z}{z_0}\right)^{\alpha} e^{-\alpha z/z_0} \,, \qquad (6)$$

where $z_0 = 0.33$ and $\alpha = 0.37$, and n_0 is a constant to normalize the distribution to unity. The function is given by the red line of Fig. 3. We refer the interested readers to our previous paper Planck Collaboration XIX (2014) to know more details of the possible systematic effects of the samples.

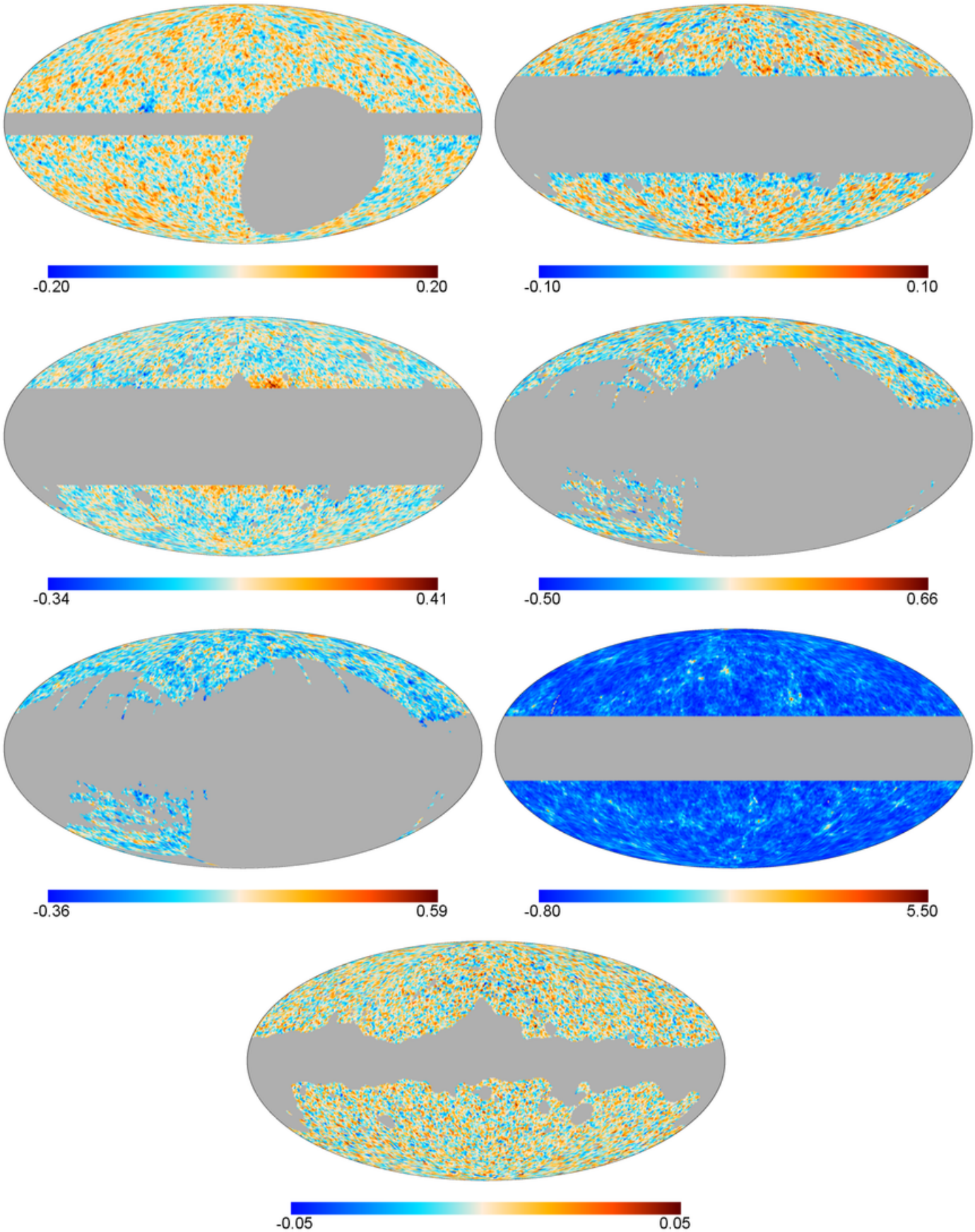

Fig. 4. Density contrast maps obtained from the galaxy catalogues at $N_{\rm side} = 64$. From left to right and from top to bottom: NVSS, WISE-AGN, WISE-GAL, SDSS-CMASS/LOWZ, SDSS-MphG, and 2MPZ. The *Planck* lensing convergence map (Kappa) is given in the fourth row. For visualization purposes, all these maps are Wiener-filtered versions of the original data. Maps are dimensionless.

Table 1. Main characteristics of the galaxy catalogues used as tracers of the gravitational potential. From left to right, the columns indicate the number of galaxies per steradian, the fraction of the sky covered by each survey, the galaxy redshift distribution, the galaxy bias, and the mean redshift.

Galaxy catalogue	$\bar{n}$	$f_{\rm sky}$	dn/dz	bias	$\bar{z}$
NVSS	1.584×10^5	0.73	$\propto (z/0.33)^{0.33}\, e^{-0.37(z/0.33)}$	$0.90\left(1+0.54\,(1+z)^2\right)$	1.22
WISE-AGN	1.552×10^5	0.45	numerical	$0.48\left(1+0.54\,(1+z)^2\right)$	1.03
WISE-GAL	1.187×10^7	0.45	numerical	$0.79\,(1+z)$	0.38
SDSS-CMASS/LOWZ	5.558×10^5	0.22	numerical	2.03	0.45
SDSS-MphG	9.680×10^6	0.22	$\propto (z/0.16)^{1.5}\, e^{(-z/0.34)^{2.30}}$	1.20	0.32
2MPZ	8.328×10^4	0.66	numerical	1.35	0.09

2.2.2. The *Sloan Digital Sky Survey* catalogues

We use two sub-samples of SDSS: the SDSS luminous galaxy samples (SDSS-CMASS/LOWZ) and the main photometric SDSS galaxy sample (SDSS-MphG). The redshift distributions of the two samples are shown in blue and green lines in Fig. 3. Their sky coverage is shown in the sub-plots of Fig. 4, and the angular power spectrum in the sub-plots of Fig. 5.

SDSS-CMASS/LOWZ

We use the photometric luminous galaxy (LG) catalogue from the Baryonic Oscillation Spectroscopic Survey (BOSS) of the SDSS III. The data used consist of two sub-samples: CMASS and LOWZ. In this paper we will use the combination of them, i.e., SDSS-CMASS/LOWZ in our data analysis.

The CMASS sample has roughly constant stellar mass, and is mostly contained in the redshift range $z = 0.4$–0.7, with a galaxy number density close to $110\,\mathrm{deg}^{-2}$. With the colour selection criteria it is a catalogue of about one million sources, in an area of $10{,}500\,\mathrm{deg}^2$. Photometric redshifts of this sample are calibrated using a selection of about 100,000 BOSS spectra as a training sample for the photometric catalogue.

The photometric LOWZ samples are selected luminous, highly biased, mostly red galaxies, placed at an average redshift of $\bar{z} \approx 0.3$ and below the redshifts of the CMASS sample ($z < 0.4$). With a total number of sources of roughly 600,000, the number density of galaxies in the southern part of the footprint is higher than in the northern one (by more than 3 %). Both SDSS-CMASS and SDSS-LOWZ samples are further corrected for any scaling introduced by possible systematics like stars, mask value, seeing, sky emission, air mass and dust extinction, since the high star density tend to "blind" galaxy detection algorithms. The algorithm followed to correct for systematics is described in Hernández-Monteagudo et al. (2013).

SDSS-MphG

These are the photometrically-selected galaxies from the SDSS-DR8 catalogue, which covers a total sky area of $14{,}555\,\mathrm{deg}^2$ (Aihara et al. 2011). The total number of objects labelled as galaxies in this data release is 208 million. But for correcting extinction and restricting redshift ranges, our final sample consists of about 42 million, with redshifts distributed around a median value of ≈ 0.35. We use the analytical function

$$\frac{dn}{dz} = \frac{\beta}{\Gamma\left(\frac{m+1}{\beta}\right)} \frac{z^m}{z_0^{m+1}} e^{-(z/z_0)^\beta}\,, \tag{7}$$

with parameters $m = 1.5$, $\beta = 2.3$ and $z_0 = 0.34$ for the number density distribution, and the constant galaxy bias $b = 1.2$ by fitting the ΛCDM prediction to the observed auto-correlation function of the galaxies. As for the LOWZ/CMASS LRG samples, this galaxy sample was also corrected for systematics following the approach of Hernández-Monteagudo et al. (2013).

2.2.3. The *Wide-Field Infrared Survey Explorer* extragalactic catalogues

We next describe the use of the extragalactic sources detected by the *Wide-Field Infrared Survey Explorer*, (WISE, see Wright et al. 2010) in our ISW studies. The WISE survey scanned the full sky at 3.4, 4.6, 12 and 22 μm (which constitute bands W1 to W4). These observations provide a deeper view of the infrared sky than previous surveys like 2MASS or IRAS, and provide an extensive extragalactic catalogue of more than 500 million sources (see Wright et al. 2010). The four W1 to W4 bands are sensitive to either UV radiation reproduced by dust grains in star forming galaxies or to infrared emission from stars, either in our Galaxy or in extragalactic sources. The W1 band turns out to be the deepest, sampling the deep universe by detecting massive galaxies up to $z \approx 1$ and with a median redshift of 0.3 (Yan et al. 2013)

In the context of ISW studies, our approach is very similar to that of Ferraro et al. (2014). We focus our efforts on two different sets of extragalactic sources: star forming galaxies and AGNs, and this requires a careful separation of the stars in the catalogue. Since the sky scanning of the WISE satellite is not homogeneous, a magnitude cut of W1< 16.6 is imposed to all sources at high galactic latitude, since for this cut Ferraro et al. (2014) found a uniform sample. Given that stray light from the moon may cause faint detections and other spurious effects in the data, we discard all sources with a flat `moon_lev` > 4, while also dropping all sources suspected of being artefacts (`cc_flags`≠ 0).

Following the colour cuts given in Yan et al. (2013) and Ferraro et al. (2014), we impose the cut W1-W2> 0 to isolate the galaxies from stars, while the stricter conditions W1-W2> 0.85 and W2<15.0 should separate the AGNs from star forming galaxies, although the former constitute a very small fraction of the latter: with these cuts, we obtain about 140 million galaxies and 1.4 million AGNs in the entire sky.

The presence of systematics causes clear excess in the auto-power spectra of these two WISE-based surveys on the largest scales. This poses a problem since, in order to predict the level of cross-correlation with the CMB maps generated by the ISW component, we need first to characterise the bias of each tracer. For this purpose we follow exactly the same approach as in Ferraro et al. (2014): we use the cross-correlation of these two galaxy surveys with lensing convergence maps from *Planck* in order to estimate the bias. This requires adopting some models for the redshift distribution of WISE galaxies and AGNs, and in

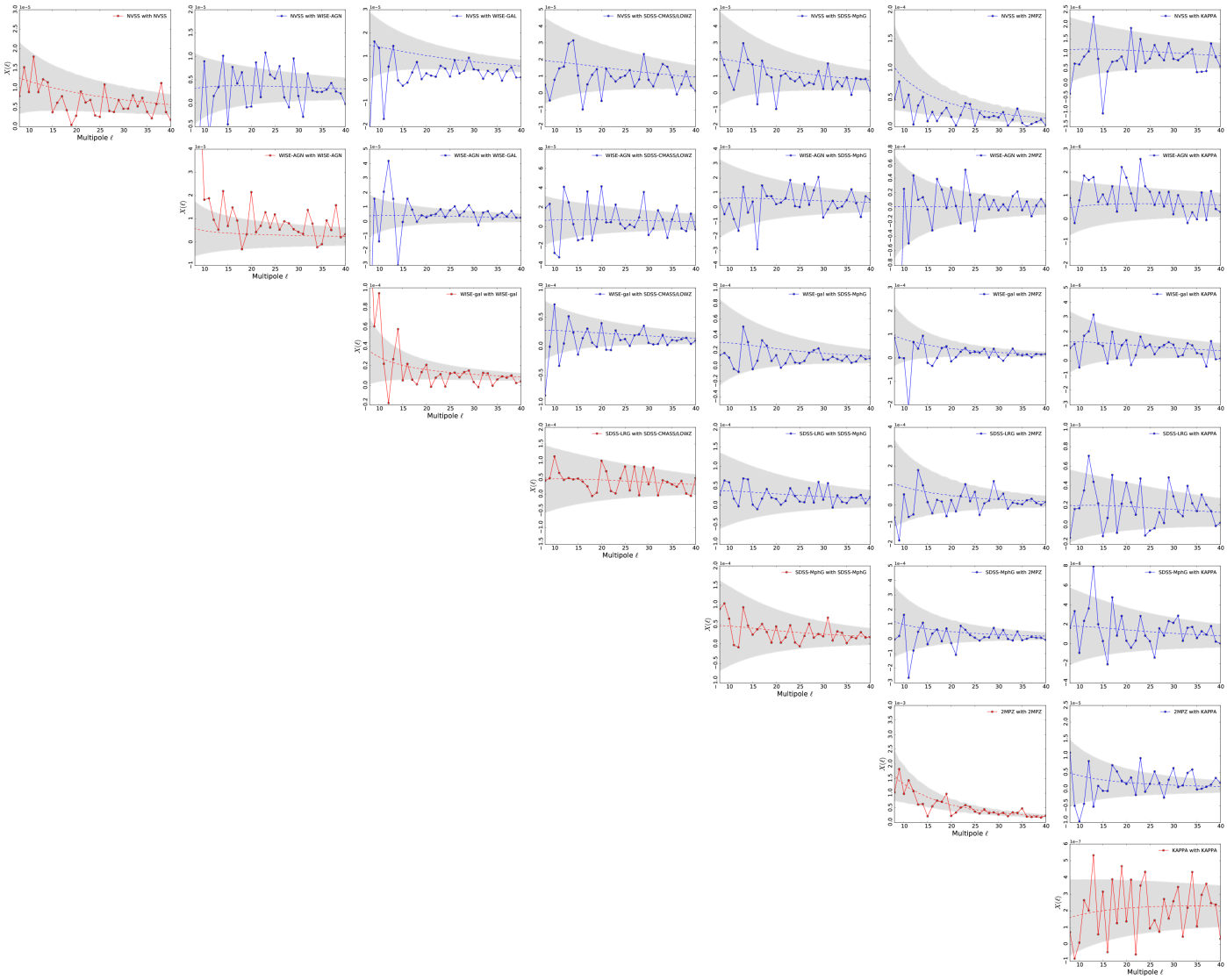

Fig. 5. Angular power spectra from the maps in Fig. 4. From top to bottom: NVSS, SDSS-CMASS/LOWZ, SDSS-MphG, WISE-GAL, WISE-AGN, 2MPZ, and Kappa. The observed spectra are the points (red for auto spectra and blue for the cross spectra), while the theoretical models are represented by the dashed lines (the grey areas correspond to the sampling variance).

particular we use those given in Yan et al. (2013), which were obtained after cross-matching WISE and SDSS data. We also adopt some redshift dependences for the bias which are identical to those used in Ferraro et al. (2014) For WISE-GAL our fiducial model has this very simple redshift dependence:

$$b^{\rm WISE-GAL}(z) = b_0^{\rm WISE-GAL}(1+z)\,, \qquad (8)$$

while for the WISE-AGN the suggested redshift dependence is quadratic

$$b^{\rm WISE-AGN}(z) = b_0^{\rm WISE-AGN}[0.53 + 0.289(1+z)^2], \qquad (9)$$

After cross-correlating with *Planck* lensing convergence maps in the multipole range $\ell \in [10, 400]$, we find the following values for the fiducial parameters: $b_0^{\rm WISE-GAL} \simeq 0.79$, and $b_0^{\rm WISE-AGN} \simeq 0.90$.

2.2.4. The 2MASS Photometric Redshift catalogue

The 2MASS Photometric Redshift catalogue (hereafter 2MPZ Bilicki et al. 2014) is a combination of the 2MASS XSC (Jarrett et al. 2000), WISE, and SuperCOSMOS (Hambly et al. 2001) surveys yielding an all sky extragalactic source catalogue with a typical uncertainty in redshift of $\sigma_z = 0.016$. This is achieved by employing an artificial neural network approach (the ANNz algorithm, see Collister & Lahav 2004) on the above quoted surveys, and after training it with the 2MRS (Huchra et al. 2012), SDSS[2], 6dFGS (Jones et al. 2009), 2dFGRS[3] and ZCAT (Huchra et al. 1995) spectroscopic surveys.

The resulting catalogue contains almost one million sources with a median redshift of 0.08. Out of those sources, more than three hundred thousand contain spectroscopic redshifts. In Fig. 3 we display the histogram of the photometric redshift distribution of these sources, with a high redshift tail extending up to $z \approx 0.3$. When using `MASTER` (Hivon et al. 2002) to compute its angular power spectrum, we find that its effective linear bias for large scales ($\ell < 70$) is close to unity ($b_g \simeq 1.35$). However, at small scales there is a clear evidence for non-linear power.

[2] URL site: `http://www.sdss.org`
[3] URL site: `http://www2.aao.gov.au/~TDFgg/`

2.2.5. *Planck* lensing map

The matter distribution forming the cosmic web modifies the 2D projected distribution of the CMB anisotropies on the sky, via the weak gravitational lensing effect. This distortion breaks the isotropy of the intrinsic CMB fluctuations, introducing correlations among multipoles. Optimal inversion methods (Hu & Okamoto 2002; Okamoto & Hu 2003) allows to recover the projected density field (ϕ), which is proportional to the gravitational field (Φ).

As part of its official products release, *Planck* provides a map of the estimated lensing field (Planck Collaboration XV 2015), that can be used to probe the ISW effect, through its cross-correlation with the CMB map, in the same manner as it is done with external galaxy catalogues. The lensing signal measured from this map is detected at $\approx 40\,\sigma$, using the full-mission temperature and polarization data to construct the lensing map estimation.

In fact, what *Planck* releases is the lensing convergence Kappa map (κ), which has a whiter angular power spectrum than the raw lensing potential (ϕ): $\kappa_{\ell m} = \phi_{\ell m}\ell(\ell+1)/2$. This lensing map was obtained from the SMICA CMB solution, and it is shown (Wiener-filtered) in Fig. 4, bottom row. It covers 67% of the sky, and a multipole range: $8 \leq \ell \leq 2048$. The convergence map traces matter distribution through a wide redshift range (see Fig. 3).

2.2.6. The *Sloan Digital Sky Survey* superstructures

We use here the catalogue of superstructures[4] from Granett et al. (2008a), also used in Planck Collaboration XIX (2014). This sample consists of 50 superclusters and 50 supervoids identified from the Luminous Red Galaxies (LRGs) in the SDSS (sixth data release, DR6, Adelman-McCarthy et al. 2008) that covers an area of 7500 deg^2 on the sky. They used publicly available algorithms, based on the Voronoi tessellation, to find 2836 superclusters (using VOBOZ, VOronoi BOund Zones, Neyrinck et al. 2005) and 631 supervoids (using ZOBOV, ZOnes Bordering On Voidness, Neyrinck 2008) above a $2\,\sigma$ significance level (defined as the probability of obtaining, in a uniform Poissonian point sample, the same density contrasts as those of clusters and voids).

The 50 superclusters and 50 supervoids they published in their catalogue correspond to density contrasts of about $3\,\sigma$ and $3.3\,\sigma$ respectively. They span a redshift range of $0.4 < z < 0.75$, with a median of around 0.5, and inhabit a volume of about $5\,h^{-3}$ Gpc^3. These superstructures can potentially produce measurable ISW signals, as suggested in Granett et al. (2008a,b). For each structure, the catalogue provides: the position on the sky of its centre; the mean and maximum angular distance between the galaxies in the structure and its centre; the physical volume; and three different measures of the density contrast (calculated from all its Voronoi cells, from only its over- or under-dense cells, and from only its most over- or under-dense cell).

2.3. Simulations

We have performed 11,000 coherent simulations of the CMB and different LSS tracers, which are used to study the CMB-LSS cross-correlation up to $\ell \approx 190$, in fact, the maps are produced directly at $N_{\rm side}$= 64, since we have checked that these maps already capture all the information required for our analyses. From the CMB side, each simulation consists in two independent signals: an ISW map and the reminder CMB anisotropies in a T map. Notice that, since no polarization information at the largest scales is provided in this release, this signal is not generated. From the galaxy-surveys side, we simulate galaxy density maps for NVSS, SDSS-CMASS/LOWZ, SDSS-MphG, WISE-AGN, and WISE-GAL. Although it is not used for studying the CMB-LSS cross-correlation, we also generate a 2MPZ map that helps to assess the quality of the ISW recovery from this photometric catalogue (see Sect. 5). Finally, we also produce a coherent lensing convergence (Kappa) map.

The maps are simulated by assuming that they are Gaussian. This is a good approximation for the Kappa map, as well as for all the distributed galaxy density maps. In particular, for the galaxy catalogues, although they follow a Poisson distribution, the mean number of galaxies per pixel is large enough (≈ 40, for the worst case: 2MPZ). Therefore, all the required information to perform the coherent simulations is given by all the auto- and cross- angular power spectra (see, for instance, Barreiro et al. 2008, for details). In particular, given two surveys a and b, the theoretical cross-angular power spectra between the surveys read as:

$$C_\ell^{ab} = 4\pi \int \frac{\mathrm{d}k}{k}\, \Delta^2(k) I_\ell^a(k) I_\ell^b(k)\,, \tag{10}$$

where $\Delta^2(k)$ is the matter power spectrum per logarithmic interval, and $I_\ell^a(k)$ is a transfer function represented by the redshift integral:

$$I_\ell^a(k) = \int_0^\infty \mathrm{d}z\; W_a(z,k)\, j_\ell(kr(z))\,. \tag{11}$$

Here $r(z)$ is the comoving distance as a function of the redshift, and j_ℓ are the spherical Bessel functions, which project the window function $W_a(z,k)$ into each multipole ℓ of the power spectrum. In the case of a galaxy-survey, the window function is independent of k and it is given by

$$W_a(z) = b_a(z) D_+(z) \frac{\mathrm{d}n_a}{\mathrm{d}z}\,. \tag{12}$$

It depends on the galaxy redshift distribution and the bias function $b_a(z)$ of each survey. The growth factor $D_+(z)$ in this expression takes into account the linear evolution of the matter perturbations.

For lensing, the efficiency window function $W_\kappa(\chi)$ which relates the density perturbations δ to the weak lensing convergence Kappa in a line of sight integration,

$$\kappa = \int \mathrm{d}\chi\; W_\kappa(\chi)\delta \tag{13}$$

is given by

$$W_\kappa(\chi) = \frac{3\Omega_m}{2\chi_H^2}\frac{D_+}{a}\frac{\chi}{\chi_{\rm CMB}}\left(\chi_{\rm CMB}-\chi\right), \tag{14}$$

with the comoving distance $\chi_{\rm CMB}$ to the surface of last scattering, which is approximately 10 Gpc/h in the ΛCDM cosmology considered here. $\chi_H = c/H_0$ is again the Hubble distance. For being able to compare the lensing efficiency function $W_\kappa(\chi)$ to the redshift distributions of other LSS surveys, we convert it by analogy into a dimensionless function by multiplying it by the inverse Hubble-function:

$$W_\kappa(z)\mathrm{d}z = W_\kappa(\chi)\mathrm{d}\chi \;\rightarrow\; W_\kappa(z) = W_\kappa(\chi)\frac{\mathrm{d}\chi}{\mathrm{d}z} = W_\kappa(\chi)\frac{c}{H(z)}. \tag{15}$$

[4] Available at http://ifa.hawaii.edu/cosmowave/supervoids/.

For the ISW effect, the window function involves the evolution of the potential with redshift:

$$W_{ISW}(z,k) = -3\Omega_m \left(\frac{H_0}{ck}\right)^2 \frac{\mathrm{d}}{\mathrm{d}z}\left[(1+z)D_+(z)\right] \ . \qquad (16)$$

It depends on k due to the Poisson equation relating the matter and the potential. If the Universe is matter-dominated, then the function $(1+z)D_+(z)$ is constant and the ISW vanishes.

All the angular power spectra used in the present paper have been calculated using a modified version of the CAMB[5] code. The fiducial ΛCDM cosmological model assumed is: $\Omega_b h^2 = 0.0222$, $\Omega_c h^2 = 0.199$, $\Omega_\nu h^2 = 0$, $\Omega_k = 0$, $n_s = 0.9615$, $A_s = 2.1740 \times 10^{-9}$, $\tau = 0.077$, and $h = H_0/100\ \mathrm{km\,s^{-1}Mpc^{-1}}$, fully compatible with the *Planck* fiducial model (Planck Collaboration XIII 2015).

3. CMB correlation with tracers of the gravitational potential

The CMB cross-correlation with LSS tracers of the matter distribution is the most classical approach to study the IWS effect: it offers the possibility of extracting these secondary anisotropies, otherwise covered by the primordial CMB anisotropies. The seminal work by Crittenden & Turok (1996) proposed to use a galaxy catalogue as LSS tracer, and the first positive detection following this approach was done by Boughn & Crittenden (2004) using *WMAP* data and radio and *X*-ray tracers. As discussed in the Introduction, several other works came after it, confirming the detection of the ISW effect with additional galaxy tracers.

In our past work (Planck Collaboration XIX 2014), we performed, for the first time, the detection of the ISW using only CMB data, by cross-correlating the *Planck* CMB map with the *Planck* lensing potential map, which is naturally used as a tracer of the matter distribution. This cross-correlation is nothing but an estimator of the ISW-lensing bispectrum induced on the Gaussian CMB anisotropies by the deflection caused by the lensing effect (see e.g., Lewis et al. 2011).

This cross-correlation has been studied using different tools: the cross-correlation function (CCF), the covariance of wavelet coefficients (Wcov), and the cross-angular power spectrum (CAPS). These three estimators were first compared in Vielva et al. (2006), and were also applied to study the cross-correlation of the *Planck* CMB data with several surveys in Planck Collaboration XIX (2014).

The CAPS is the most natural tool for studying the cross-correlation, since the entire cross-correlation signal is fully included on it. In theory, the CCF and the Wcov estimators are also optimal, as long as they are evaluated at a sufficient number of angles/scales. In fact, for a given case, the CFF and the Wcov, using a relatively small number of evaluations, can achieve a significant fraction of the total signal-to-noise. The clear advantage of CAPS is that, under certain conditions, it provides statistics with uncorrelated elements in case that full-sky maps can be used. Even for incomplete-sky signals, a pseudo angular spectrum, obtained through *a la* `MASTER` approach (e.g., Hivon et al. 2002; Hinshaw et al. 2003), provides a very good approximation to our problem.

We showed in Planck Collaboration XIX (2014) that the three estimators (CCF, Wcov and CAPS) render a similar detection level, although the CAPS obtained tighter limits than the other two approaches (specially as compared to the CCF). For that reason, in this release we only use the CAPS estimator. The measured CAPS between `SEVEM` and the LSS tracers considered in this analysis (NVSS, WISE-AGN, WISE-GAL, SDSS-CMASS/LOWZ, SDSS-MphG, and Kappa) are shown in Fig. 6.

3.1. Methodology

We aim to study the ISW cross-correlation by estimating the best-fit amplitude of the CAPS to a given fiducial model (the one mentioned in Sect. 2.3). This approach allows us to check the compatibility of the data with the ISW effect, and provides an estimate of the signal-to-noise ratio of the measured signal. This approach is complementary to an alternative approach, in which the signal is compared to the null hypothesis of no correlation between the CMB and the LSS. Using a Bayesian hypothesis test, we showed in Planck Collaboration XIX (2014) a clear evidence in favour of the alternative hypothesis as compared to the null one.

Let us denote the expected CAPS of two maps (x and y) by ξ_ℓ^{xy}, where ℓ represents a given multipole, and we assume that the two signals are given in terms of a fluctuation field (i.e., with zero mean and dimensionless).

In our particular case, x can be seen as the CMB signal, and y accounts for one or more surveys. In other words, we can pursuit the estimation of the ISW amplitude by a single correlation of the CMB with a given survey, or with several surveys jointly. In this latter case, ξ_ℓ^{xy} is a vector of $\ell_{\rm max}$ components, where the first $\ell_{\rm max_1}$ components correspond to the CMB cross-correlation with the first survey, the next $\ell_{\rm max_2}$ components correspond to the correlation with the second survey, and so on. Obviously, when $x \equiv y$, ξ_ℓ^{xy} represents an auto-correlation.

The full description of ξ_ℓ^{xy} and its covariance $\mathbf{C}_{\xi^{xy}}$, in terms of the theoretical model and the specific sky coverage, is given in Planck Collaboration XIX (2014). Since the CAPS is a very fast estimator, in particular for the $N_{\rm side}$= 64 resolution parameter, it is also possible to determine these quantities from the coherent simulations described in Sect. 2.3: we use 10 000 out of the 11 000 performed simulations to estimate both the expected signal (ξ_ℓ^{xy}) and its covariance ($\mathbf{C}_{\xi^{xy}}$). This is the approach followed in the past *Planck* release, and it is also the one adopted in this work.

Therefore, denoting the observed cross-correlation by $\hat{\xi}_\ell^{xy}$, a simple χ^2 can be proposed to estimate the amplitude A, such that $A \times \xi_\ell^{xy}$ is the best-fit solution to $\hat{\xi}_\ell^{xy}$:

$$\chi^2(A) = \left[\hat{\xi}_\ell^{xy} - A \times \xi_\ell^{xy}\right]^{\rm T} \mathsf{C}_{\xi^{xy}}^{-1} \left[\hat{\xi}_\ell^{xy} - A \times \xi_\ell^{xy}\right], \qquad (17)$$

where $\mathsf{C}_{\xi^{xy}}$ is the covariance matrix (of dimension $\ell_{\rm max} \times \ell_{\rm max}$) of the expected cross-correlation ξ_ℓ^{xy}, that is, $\mathbf{C}_{\xi^{xy}{}_{i,j}} \equiv \left\langle \xi_{\ell_i}^{xy} \xi_{\ell_j}^{xy} \right\rangle$. It is straightforward to show that the best-fit amplitude A, its error, and the significance are given by

$$\begin{aligned} A &= \left[\hat{\xi}_\ell^{xy}\right]^t \mathsf{C}_{\xi^{xy}}^{-1} \xi_\ell^{xy} \left[\left[\xi_\ell^{xy}\right]^t \mathsf{C}_{\xi^{xy}}^{-1} \xi_\ell^{xy}\right]^{-1}, \qquad (18)\\ \sigma_A &= \left[\left[\xi_\ell^{xy}\right]^t \mathsf{C}_{\xi^{xy}}^{-1} \xi_\ell^{xy}\right]^{-1/2},\\ A/\sigma_A &= \left[\hat{\xi}_\ell^{xy}\right]^t \mathsf{C}_{\xi^{xy}}^{-1} \xi_\ell^{xy} \left[\left[\xi_\ell^{xy}\right]^t \mathsf{C}_{\xi^{xy}}^{-1} \xi_\ell^{xy}\right]^{-1/2}. \end{aligned}$$

[5] http://camb.info

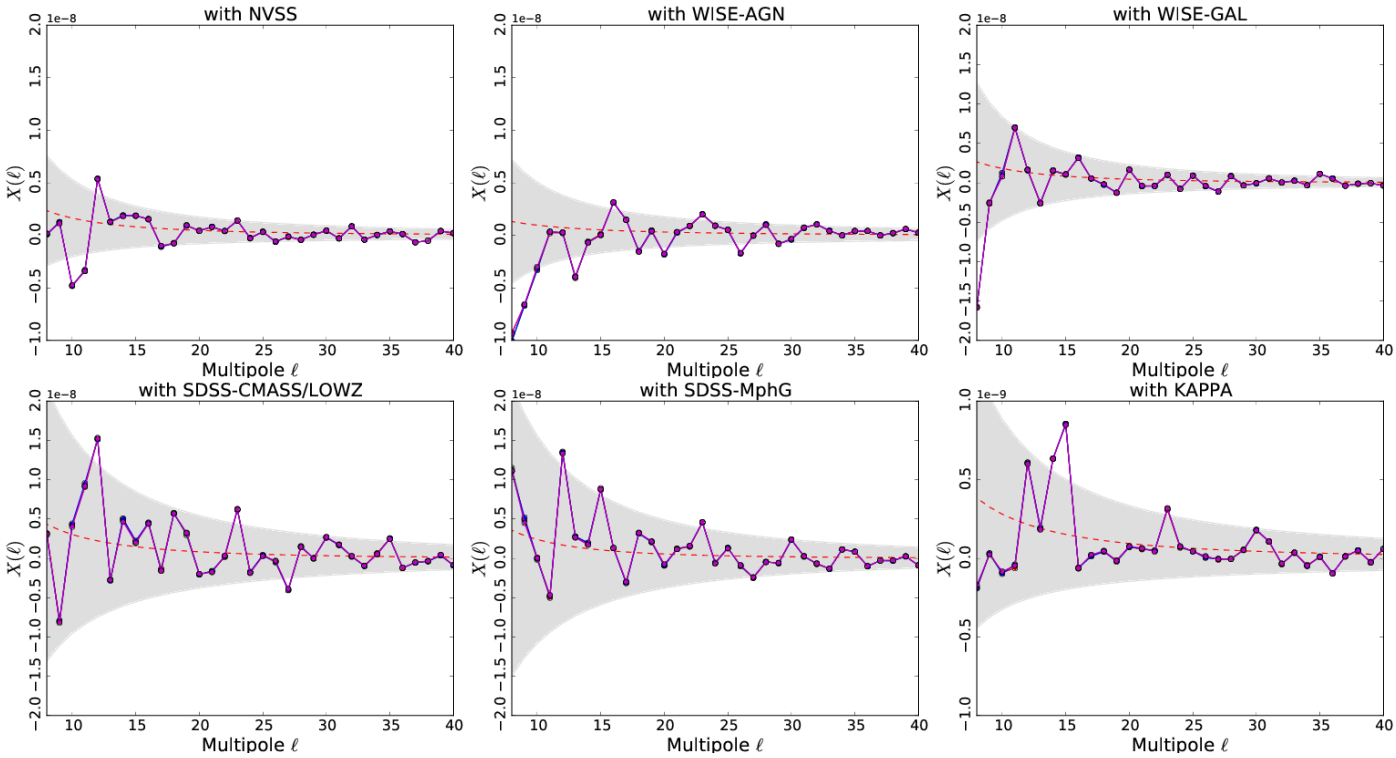

Fig. 6. Measured ISW-LSS cross-spectra (CAPS). From left to right, from top to bottom, the panels show the cross-correlation of the SEVEM CMB map with NVSS, WISE-AGN, WISE-GAL, SDSS-CMASS/LOWZ, SDSS-MphG, and Kappa. Grey area represents $1\,\sigma$ uncertainity derived from simulations. Spectra derived from the other *Planck* CMB maps are virtually the same.

Table 2. ISW amplitudes A, errors σ_A, and significance levels S/N = A/σ_A of the CMB-LSS cross-correlation (survey-by-survey and for different combinations). These values are reported for the four *Planck* CMB maps: COMMANDER, NILC, SEVEM, and SMICA. The last column stands for the expected S/N within the fiducial ΛCDM model.

LSS data	COMMANDER		NILC		SEVEM		SMICA		Expected
	$A \pm \sigma_A$	S/N	$A \pm \sigma_A$	S/N	$A \pm \sigma_A$	S/N	$A \pm \sigma_A$	S/N	S/N
NVSS	0.95 ± 0.36	2.61	0.94 ± 0.36	2.59	0.95 ± 0.36	2.62	0.95 ± 0.36	2.61	2.78
WISE-AGN ($\ell_{\rm min} \geq 9$)	0.95 ± 0.60	1.58	0.96 ± 0.60	1.59	0.95 ± 0.60	1.58	1.00 ± 0.60	1.66	1.67
WISE-GAL ($\ell_{\rm min} \geq 9$)	0.73 ± 0.53	1.37	0.72 ± 0.53	1.35	0.74 ± 0.53	1.38	0.77 ± 0.53	1.44	1.89
SDSS-CMASS/LOWZ	1.37 ± 0.56	2.42	1.36 ± 0.56	2.40	1.37 ± 0.56	2.43	1.37 ± 0.56	2.44	1.79
SDSS-MphG	1.60 ± 0.68	2.34	1.59 ± 0.68	2.34	1.61 ± 0.68	2.36	1.62 ± 0.68	2.38	1.47
Kappa ($\ell_{\rm min} \geq 8$)	1.04 ± 0.33	3.15	1.04 ± 0.33	3.16	1.05 ± 0.33	3.17	1.06 ± 0.33	3.20	3.03
NVSS and Kappa	1.04 ± 0.28	3.79	1.04 ± 0.28	3.78	1.05 ± 0.28	3.81	1.05 ± 0.28	3.81	3.57
WISE	0.84 ± 0.45	1.88	0.84 ± 0.45	1.88	0.84 ± 0.45	1.88	0.88 ± 0.45	1.97	2.22
SDSS	1.49 ± 0.55	2.73	1.48 ± 0.55	2.70	1.50 ± 0.55	2.74	1.50 ± 0.55	2.74	1.82
NVSS and WISE and SDSS	0.89 ± 0.31	2.87	0.89 ± 0.31	2.87	0.89 ± 0.31	2.87	0.90 ± 0.31	2.90	3.22
All	1.00 ± 0.25	4.00	0.99 ± 0.25	3.96	1.00 ± 0.25	4.00	1.00 ± 0.25	4.00	4.00

3.2. Cross-correlation results

The fundamental CMB-LSS cross-correlation results are summarized in Table 2, where we report the estimated ISW amplitude (A), its error (σ_A), and the detection level A/σ_A, derived for the surveys described in 2.2, applying Eqs. 18. Results obtained from the four *Planck* CMB maps (COMMANDER, NILC, SEVEM, and SMICA) are given, showing a perfect agreement among them, indicating a robust recovery of the largest CMB anisotropies.

In addition to estimate the ISW amplitude by fitting individual surveys, we also consider several combinations: NVSS and Kappa, the two SDSS surveys (SDSS-CMASS/LOWZ and SDSS-MphG), the two WISE catalogues (WISE-AGN and WISE-GAL), the five external tracers (NVSS, and WISE and SDSS surveys), and the six surveys together. As expected, the lowest error is achieved by combining all the surveys, taking into account all their mutual correlations. For the fiducial ΛCDM

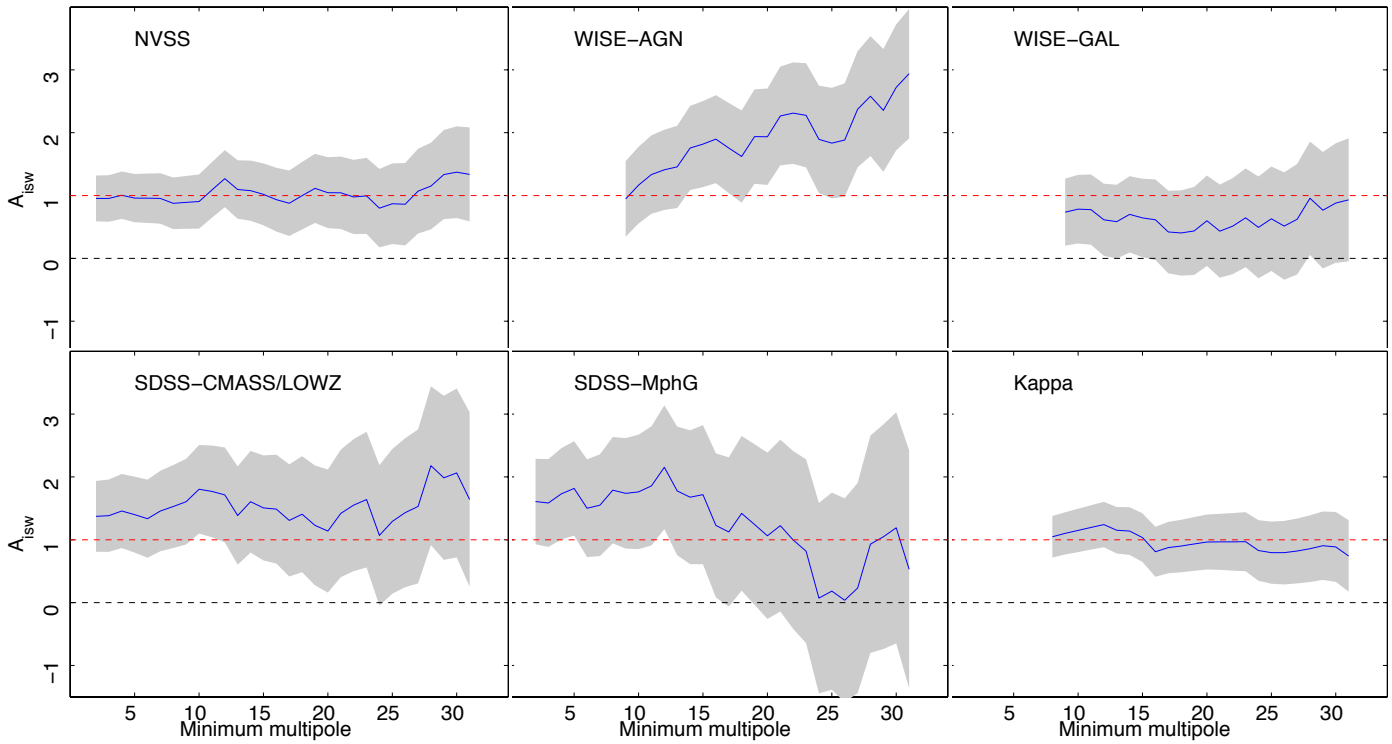

Fig. 7. Dependence of the estimated $A_{\rm ISW}$ amplitude for the different surveys as a function of the $\ell_{\rm min}$ considered in the amplitude estimation.

model a total signal-to-noise of $4\,\sigma$ is predicted, and, that is the actual value estimated from the data.

The highest contribution comes from the *Planck* convergence lensing map (Kappa), which provides a detection level of $3.2\,\sigma$, followed by NVSS thats allows to detect the ISW effect at $2.6\,\sigma$. In fact, the combination of these two LSS tracers almost provide the full detection achieved with the six surveys: $3.8\,\sigma$.

The ISW signal characterized from the SDSS catalogues has a signal-to-noise level of around $2.4\,\sigma$ for each survey, and $2.7\,\sigma$ when they are considered jointly. The WISE surveys provide the lowest signal-to-noise: $1.6\,\sigma$ for WISE-AGN, $1.4\,\sigma$ for WISE-GAL, and $1.9\,\sigma$ for the combination of both. The signal-to-noise achieved by the combination of the five external tracers is $2.9\,\sigma$. All these detection levels refer to `SEVEM`, although the ones achieved from the analysis of the other *Planck* CMB maps are virtually the same.

All the estimated amplitudes are compatible with unity, within the corresponding 1σ level. In fact, the value of the ISW amplitude is quite stable, independently of which is the lowest multipole ($\ell_{\rm min}$) considered in the amplitude estimation. This is graphically represented in Fig. 7, where the best-fit amplitude A (solid-blue lines) and its 1σ error (grey areas) are shown. It is remarkable that the estimated amplitude is very constant as a function of $\ell_{\rm min}$, and compatible with unity. The only case in which there is a certain incompatibility is for WISE-AGN, where, for $\ell_{\rm min} \gtrsim 18$, the departure from unity is in tension at 1σ. This could be the indication of some systematics or contamination, still present in this catalogue.

Another interesting aspect is shown in Fig. 8, where the correlation between ISW amplitudes is given, for all the possible survey-survey combinations. Using our coherent simulations, we have studied which is the correlation coefficient (ρ) among the estimated A amplitudes from each one of the six surveys. On each panel of this figure, we show a scatter plot obtained from 1,000 simulations, confronting the ISW estimation for two surveys. We also plot (red circle) the value corresponding to the data. Finally, the correlation coefficient is also given.

As it can be seen, the highest correlation occurs between the two SDSS catalogues ($\rho = 0.66$), followed by the mutual correlations among NVSS, WISE-GAL, and SDSS-MphG ($\rho \approx 0.38$). The lowest degree of correlation occurs between WISE-AGN and the two SDSS catalogues ($\rho = 0.08$). The amplitude estimations obtained from the data are in excellent agreement with the scatter plots, where, perhaps, the highest tension is due to the SDSS-MphG catalogue, whose estimated amplitude is slightly high, although compatible at the 1σ level.

As previously mentioned, the CMB-Kappa cross-correlation is one of the most robust results, since it represents a detection of the ISW effect, fully obtained from *Planck* data, which simplifies possible sources of systematics present on galaxy catalogues. This correlation is nothing but an estimation of the ISW-lensing bispectrum (Lewis et al. 2011) induced by the lensing effect suffered from the CMB photons, as they pass through the gravitational potential.

This bispectrum represents a bias when determining some primordial bispectrum shapes, and one needs to account properly for it. Within the *Planck* collaboration, this alternative way of measuring the ISW-lensing correlation is carried out in Planck Collaboration XVII (2015). In fact, a similar cross-correlation as the one described here is also performed in the *Planck* lensing paper (Planck Collaboration XV 2015), as a sanity check to establish the goodness of the lensing map reconstruction. In the following section, we summarize these alternative ISW-lensing estimations performed within the present 2015 release.

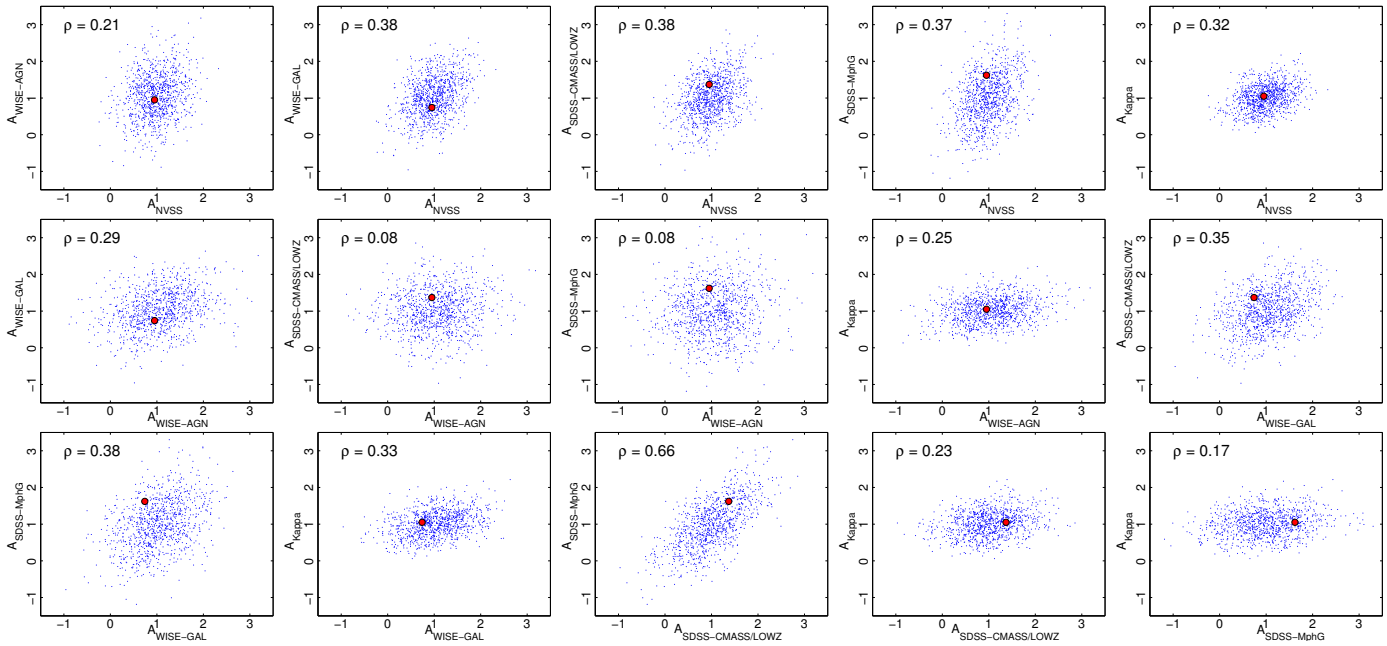

Fig. 8. Correlation among the estimated $A_{\rm ISW}$ amplitude for the different surveys. The small blue dots are the amplitudes estimated from the simulations described in Sect. 2.3, whereas the large red dot stands for the amplitudes estimated from the data. For each pair, the correlation coefficient is indicated.

3.3. Results on the ISW-lensing bispectrum

The *Planck* 2013 results Planck Collaboration XIX (2014); Planck Collaboration XVII (2014); Planck Collaboration XXIV (2014) showed for the first time evidence of the lensing-ISW CMB bispectrum by using the *Planck* 2013 temperature-only data release. The lensing-ISW non-Gaussian signal is an extremely interesting independent and direct probe of the influence of dark energy on the evolution of structure in the Universe, which only relies on CMB data.

The lensing potential ϕ and the CMB temperature T are correlated, since it is the same gravitational matter distribution at redshifts less than about 2 that leads to both the gravitational lensing of the CMB and the ISW effect. Moreover, since the gravitational lensing leads to changes in the small-scale power of the CMB, and the ISW effect affects the large-scale CMB temperature, we get a non-zero lensing-ISW bispectrum of a predominantly squeezed shape, correlating one large scale with two much smaller scales (see e.g., Goldberg & Spergel 1999; Seljak & Zaldarriaga 1999; Hu 2000; Hu & Okamoto 2002; Verde & Spergel 2002; Giovi et al. 2003; Okamoto & Hu 2003; Giovi & Baccigalupi 2005; Lewis & Challinor 2006; Serra & Cooray 2008; Mangilli & Verde 2009; Hanson et al. 2009, 2010; Smith & Zaldarriaga 2011; Lewis et al. 2011).

The 2015 release offers us the possibility of including the polarization in the estimation of the ISW-lensing bispectrum. As shown in Cooray & Melchiorri (2006), the direct ISW-lensing correlation in E-polarization due to re-scattering of the temperature quadrupole generated by the ISW effect is negligible. However, as explained in Lewis et al. (2011), there is an important correlation between the lensing potential and the large-scale E-polarization generated by scattering at reionization. Because the lensing potential is highly correlated to the ISW signal, this does in the end also lead to a non-zero ISW-lensing bispectrum in polarization. Although the effective high-pass filtering of the polarization data reduces this cross-correlation somewhat, it is in principle still detectable. Explicit expressions of the ISW-lensing bispectrum template can be found in Planck Collaboration XVII (2015).

In this section we summarize the ISW-lensing estimations performed in three different papers of the present *Planck* 2015 release, and we comment on their compatibility. First, as explained in the previous subsection, we have implemented an estimator (see Eq. 18) of the ISW-lensing bispectrum in terms of the CMB and lensing cross-correlation (Lewis et al. 2011). An independent implementation of the same estimator can be found in the *Planck Lensing* paper (Planck Collaboration XV 2015). However, whereas the latter uses the FFP8 simulations (which include the actual non-Gaussian signal induced by the lensing of the CMB anisotropies), the implementation performed in this paper uses the Gaussian simulations that form part of the set of coherent CMB and LSS tracers maps. Despite this difference, both implementations yield very similar results: the ISW paper estimator gives $A = 1.06 \pm 0.33$, whereas the lensing paper estimator finds $A = 0.90 \pm 0.28$ (both for SMICA).

The *Planck Primordial non-Gaussianity* paper (Planck Collaboration XVII 2015) studies the ISW-lensing signal primarily to determine the bias that induces on the different primordial bispectrum shapes. However, it also gives results for the actual amplitude of the ISW-lensing signal. Three different estimators have been considered in this paper: the KSW estimator (Komatsu et al. 2003), the modal estimator (Fergusson et al. 2010), and the binned bispectrum estimator (Bucher et al. 2010) (see Planck Collaboration XVII 2015, for more details on these estimators). Whereas the two former methods are only implemented to work with temperature data, the binned bispectrum estimator is also able to include polarization. All these estimators use the FFP8 simulations to characterize the expected signal and the uncertainties. The binned bispectrum estimator finds an amplitude of the ISW-lensing bispectrum of $A = 0.82 \pm 0.27$ for the SMICA map using both temperature and polarization. The values obtained using temperature alone by the KSW, modal and binned

bispectrum estimator are: $A = 0.79 \pm 0.28$, $A = 0.72 \pm 0.26$, and $A = 0.59 \pm 0.33$, respectively.

We performed a study on a set of 100 FFP8 simulations that had passed through the SMICA component separation pipeline to investigate the unbiasedness of the estimators and their correlations. For reasons explained above, the two implementations of the estimator based on the lensing reconstruction are not exactly the same. There are also differences between the three bispectrum estimators: the KSW estimator implements the ISW-lensing template exactly (since it is separable), while the modal and binned estimators use approximations. Unlike all other templates studied in Planck Collaboration XVII (2015), the ISW-lensing template is difficult to bin and the correlation between the exact and binned template is relatively low. Another difference is that the bispectrum estimators use $\ell_{\rm min} = 40$ in polarization, while the lensing reconstruction estimators use $\ell_{\rm min} = 8$. For all these reasons we do not expect the correlation between the different estimators to be perfect, which leads to slight differences in the results. The result of the study was that all the bispectrum estimators agree on the average value, which is slightly low around 0.85. The other estimators find higher values. Since these same simulations are used to determine the error bars on the final result, all the error bars have been divided by the average that each estimator finds. Regarding the correlations we find that the KSW and modal estimator are correlated at about 95%, while their correlation with the binned estimator is about 80%. The two lensing reconstruction estimators are also correlated at about 80%, while the correlation between the two types of estimator classes is about 60–70%.

Despite these differences, we can still conclude that all results are consistent with the expected value for the ISW-lensing bispectrum amplitude $A = 1$, and that the absence of any ISW-lensing signal ($A = 0$) is excluded at the level of about 3σ.

3.4. Derived cosmological constraints on dark energy

We have explored the possibility of constraining some cosmological parameters through the ISW detection reported in 3.2. In principle, the ISW effect depends on the full parameter set of a dark energy (or curvature) cosmology, but the weak overall significance of the signal makes it necessary to restrict parameter measurements to a single or at most a pair of parameters, while the remaining parameters need to be constrained from other observations.

We have assumed a Gaussian shape for the ISW likelihood $\mathcal{L}(\Theta)$, where Θ stands for a general set of cosmological parameters:

$$-2\ln[\mathcal{L}(\Theta)] = \chi^2(\Theta) - \chi^2_{\rm min}. \quad (19)$$

where the corresponding quadratic $\chi^2(\Theta)$-functional is given by:

$$\chi^2(\Theta) = \left[C_\ell^{TG,\rm obs} - C_\ell^{TG}(\Theta)\right] C^{-1}_{\ell\ell'} \left[C_{\ell'}^{TG,\rm obs} - C_{\ell'}^{TG}(\Theta)\right]. \quad (20)$$

The covariance matrix $C_{\ell\ell'}$ describes the Gaussian variation of the measured spectrum $C_\ell^{TG,obs}$ around the theoretical expectation C_ℓ^{TG}, and is estimated from the 10 000 simulations described in Sec. 2.3 and used in the cross-correlation analyses in the previous section:

$$C_{\ell\ell'}(\Theta_0) = \sum_{i=1}^{N} \frac{\Delta(C_{\ell i})\Delta(C_{\ell' j})}{N} \quad (21)$$

where $\Delta(C_{\ell i}) = C_{\ell i}^{TG}(\Theta_0) - \bar{C}_\ell^{TG}(\Theta_0)$, $C_{\ell i}^{TG}$ are the estimates for every single realization i, and the $\bar{C}_\ell^{TG}$ is their theoretical value.

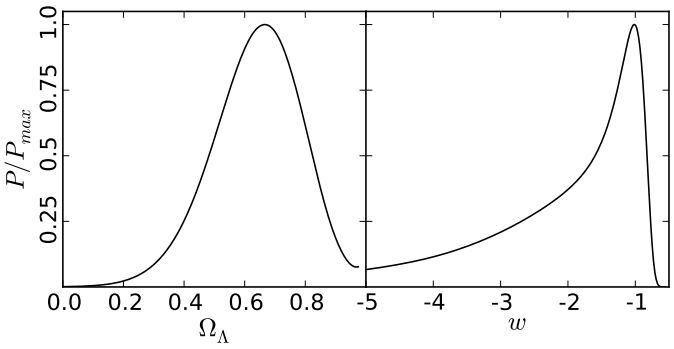

Fig. 9. Conditional probabilities on Ω_Λ (left panel) and w (right panel) derived from the ISW likelihood, based on the CMB-NVSS and the CMB-Kappa cross-correlations.

Non-zero off-diagonal entries describe correlations between different multipoles due to broken homogeneity, which is mainly caused by masking off emission from the Milky Way.

We expect that the covariance matrix does not change strongly with the cosmological model and therefore, that the fiducial model Θ_0 given in Sec. 2.3 provides a suitable uncertainty characterization for all considered cases. The Gaussian likelihood adoted above is the common choice for this effect (e.g., Nolta et al. 2004; Vielva et al. 2006; Ho et al. 2008). In our case, this likelihood is used to explore the conditional probability of a given cosmological parameter (e.g., Ω_Λ), keeping constant the remaining cosmology. In this case, it is trivial to prove that the estimator is unbiased.

For simplicity, the data used for the ISW likelihood is the joint cross-correlation of the *Planck* CMB map with the NVSS and the Kappa tracers, which already captures the 95% of the total detection of the ISW effect (see Table 2). First, we have determined the conditional probability (where the rest of the cosmological parameters are kept to the *Planck* fiducial model, Planck Collaboration XIII 2015) for Ω_Λ, obtaining the best-fit for $\Omega_\Lambda = 0.67$ and $0.49 < \Omega_\Lambda < 0.78$ at 68%. In particular, $\Omega_\Lambda > 0$ at more than $3\,\sigma$. Second, we have estimated the conditional probability on the equation of state parameter of the dark energy, obtaining the best-fit for $w = -1.01$ and $-4.45 < w < -1.07$ at 68%. These conditional probabilities are shown in Fig. 9.

4. Stacking of CMB temperature and polarization data

As an alternative approach to the detection of the ISW signal, we can focus on the objects expected to yield the strongest effect: the largest (tens to hundreds of Mpc) voids and clusters in the Universe. In order to measure the effect produced by individual structures, one can stack patches of the CMB anisotropies map centred at the location of superstructures on the sky. Such stacking technique allows to detect and characterize a signal that, otherwise, would be undetectable due to the weakness of the ISW effect compared to the primordial CMB anisotropies.

Following this approach, Granett et al. (2008a) (hereinafter GR08) found a potentially significant ISW signal by studying 100 superstructures identified in the SDSS DR6 LRG. The presence of this signal has been since confirmed and more precisely studied with the latest CMB data (Planck Collaboration XIX 2014). However, the statistical significance of this detection is still debated, as well as its supposed ISW nature

(Hernández-Monteagudo & Smith 2013; Ilić et al. 2013; Planck Collaboration XIX 2014) and the compatibility of its high amplitude with ΛCDM predictions of the ISW effect from such structures (Granett et al. 2008a; Hernández-Monteagudo & Smith 2013; Cai et al. 2014; Hotchkiss et al. 2014). Moreover, more recent and consequent catalogues of superstructures have since been used for the purpose of similar studies (Planck Collaboration XIX 2014; Kovács & Granett 2015), but none of them has yielded a signal with the same level of significance as the GR08 catalogue.

A crucial point in stacking studies is to determine whether any significant signal detected using this method is either due to the ISW effect of the observed structures, or random and fortuitous anisotropies of the primordial CMB, or a mixture or both. In the present section, we attempt to address this question for the results obtained with the GR08 catalogue, as it is up to date the only result to allegedly show a significant discrepancy with respect to ΛCDM expectations. The main originality of the present analysis compared to previous works in the literature will be the use of a variety of statistical tests which rely on the latest polarization data from the Planck satellite. Indeed, the CMB polarization map should prove to be a valuable asset for our purposes: any ISW signal found in temperature is expected to have no counterpart in CMB polarization, whereas we expect that a primordial CMB signal will be correlated at some level with the CMB polarization. Therefore, and despite the lack of the largest scales (see Sect. 2.1) in the polarization data, it can be used as a discriminant to separate genuine ISW detections from false positives due to random primordial anisotropies.

In practice, our objective here will be to answer the following questions: Can polarization data help us to prove the ISW nature of the GR08 signal? Or disprove it – i.e. show that it is actually caused (partially or entirely) by the primordial part of the CMB? We should keep in mind that the answers to these two questions could very well be negative, if the discriminating power of polarization data proves to be insufficient for stacking studies. In addition, the validity of the GR08 as a LSS tracer is also addressed by stacking patches from the *Planck* lensing map.

4.1. Stacking methodology in polarization

The main procedure for the stacking of CMB patches has been detailed in Planck Collaboration XIX (2014). However, the process for stacking patches of polarization data is not as straightforward as for scalar signals like the CMB temperature or the E mode polarization; indeed, the Q and U tensorial components are referred in a local frame, and patches at different locations cannot be directly stacked together. Here instead, we employ a configuration of the Stokes parameters which allows for superposition; more precisely, we use the following locally defined rotation of the Stokes parameters:

$$\begin{aligned} Q_{\rm r}(\boldsymbol{\theta}) &= -Q(\boldsymbol{\theta})\cos(2\phi) - U(\boldsymbol{\theta})\sin(2\phi) \\ U_{\rm r}(\boldsymbol{\theta}) &= Q(\boldsymbol{\theta})\sin(2\phi) - U(\boldsymbol{\theta})\cos(2\phi) \end{aligned} , \qquad (22)$$

where $\boldsymbol{\theta} = \theta(\cos\phi, \sin\phi)$ and ϕ is the angle defined by the line that connects the location considered at the centre of the reference system and a position at an angular distance θ from the centre. This definition, first proposed by Kamionkowski & Loeb (1997), decomposes the linear polarization into a radial ($Q_{\rm r} > 0$) and a tangential ($Q_{\rm r} < 0$) contribution around the reference positions. Komatsu et al. (2011) provided a recipe to compute the theoretical T, $Q_{\rm r}$ and $U_{\rm r}$ angular profiles from stacked patches centred on temperature peaks, making explicit its dependence on the correlations of the CMB primordial anisotropies.

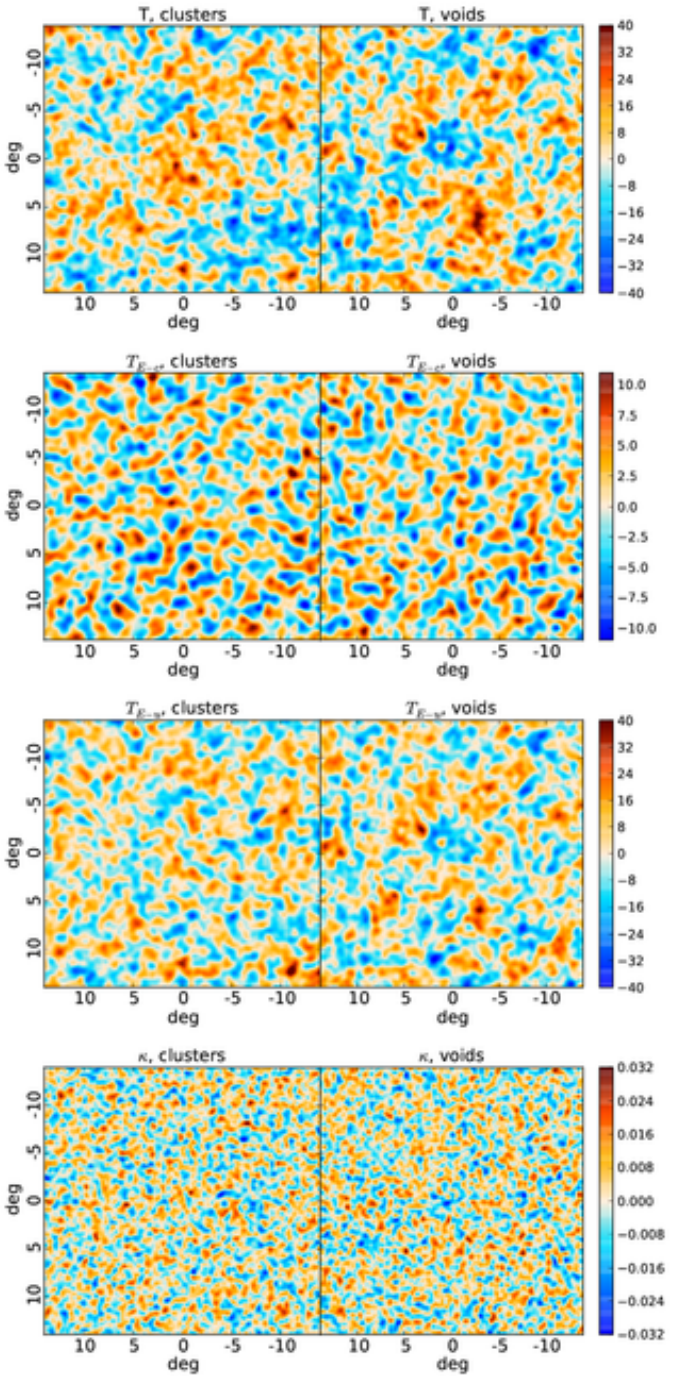

Fig. 10. Stacked patches of the scalar components from the SEVEM solution, at the superclusters (first column) and supervoids (second column) positions from GR08. From top to bottom: T, T_{E-c}, T_{E-u} and κ components. Temperature maps are given in μK units.

In practice, we also remove the monopole and dipole from the temperature maps outside the mask, before computing the $Q_{\rm r}$ signal around each location of the GR08 structures. Similarly to the work done in Planck Collaboration XIX (2014), we then compute two types of profiles from each temperature, $Q_{\rm r}$ and $U_{\rm r}$ patch. On the one hand, the radial angular profile is obtained as the mean of the pixels in rings of fixed width. We choose 150 dif-

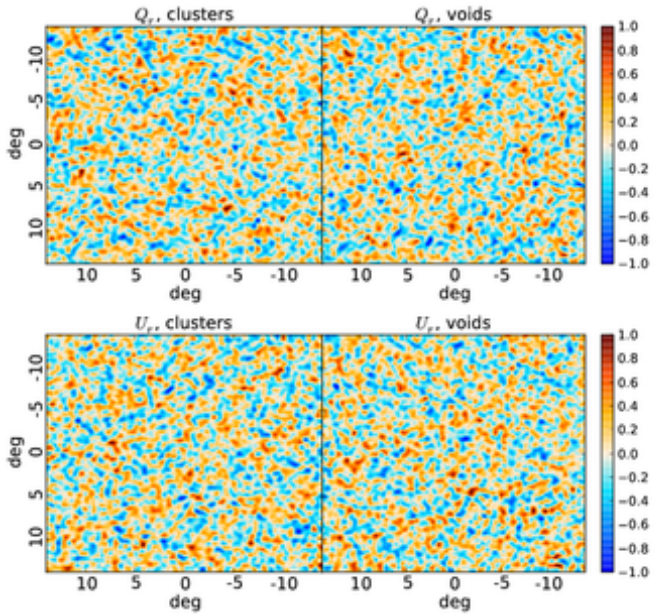

Fig. 11. Stacked patches of the Q_r and U_r components from the SEVEM solution in μK, at the superclusters (first column) and supervoids (second column) positions from GR08. From top to bottom: Q_r, U_r components in μK units

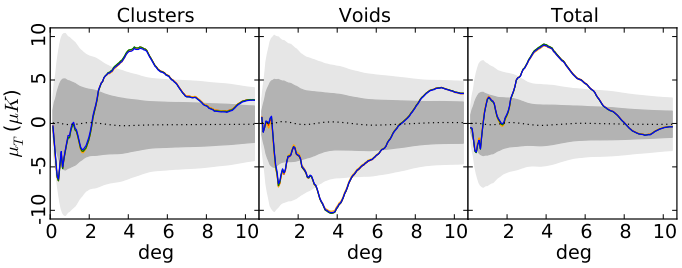

Fig. 12. Photometry profiles of the stacked temperature patches at the superclusters (first panel) or supervoids (second panel) positions from the GR08 catalogue. The third panel shows the difference between cluster and void profiles. Colour lines correspond to the different component separation methods: COMMANDER (red), NILC (orange), SEVEM (green) and SMICA (blue). The dotted black lines correspond to the mean values of the "null" profiles, i.e. computed at the same locations as the real superstructures, but in 1000 FFP8 simulations processed through the SEVEM pipeline. The shaded regions show the 1σ and 2σ error bars. Similar levels are obtained for the different component separation methods.

ferent angular scales from 0° and 15°, with a width of $\delta\theta = 0°.5$ for each ring. On the other hand, the value of the photometry profile at a given scale is defined as the difference between the average signal within the disk of radius θ and the surrounding ring of equal area (i.e. between radius θ and $\theta\sqrt{2}$). In this case, 150 angular scales are also taken into account, defining the aperture size between 0° and $15°/\sqrt{2} \simeq 10°.6$. The final step is to compute the average of all profiles (radial or photometric) for all of the selected locations.

Complementary to the temperature analysis, the stacked profiles are also computed for the E-correlated (T_{E-c}) and the E-uncorrelated (T_{E-u}) temperature maps (see Sect. 2.1), as well as for the *Planck* lensing map, where we search for a counterpart to the anomalous temperature signal. The stacked images for every map and set of structures considered in this section are shown in Figs. 10 and 11.

4.2. Temperature analysis

In order to confirm the result presented in Planck Collaboration XIX (2014), we carry out the stacking of temperature patches at the locations of the GR08 structures. For the whole analysis, we use HEALPix maps at $N_{\rm side} = 512$ with a window function of FWHM = 20 arcmin. The mean radial and photometry profiles are computed from each set of 50 superclusters and supervoids, respectively. Simultaneously, we perform the same analysis on 1000 FFP8 simulations of CMB temperature, and derive the statistical properties of the resulting profiles (mean and standard deviation at all scales). Finally, we determine if the profiles measured on real CMB data present any significant deviation from the ones derived from the simulations. Since we expect the simulated maps to have no correlation with the actual large-scale structures of the Universe, this procedure corresponds to carrying out a null hypothesis test.

As we show in Fig. 12, we observe the peculiar shape for the profiles already detected in Planck Collaboration XIX (2014) using the CMB temperature maps supplied by the different component separation methods: an excess of temperature signal at scales about 5° in the photometry profiles computed on the superclusters positions, and a deficit at scales about 4° in the corresponding supervoids locations. The deviation is even more evident if the total photometry profiles are computed as the difference between the profiles from clusters and voids, as is shown in the third panel of Fig. 12.

A multi-frequency analysis on SEVEM maps is also performed to check if these deviations are monochromatic or, conversely, show a specific frequency dependence. In Fig. 13, we show the mean temperature profiles computed in the 100 GHz, 143 GHz and 217 GHz maps. The error bars are estimated as the dispersion of the mean profiles computed at the GR08 positions in 1000 FFP8 simulations processed through the corresponding SEVEM pipeline. As we show in Fig. 13, the temperature signal is frequency independent, as already checked in Planck Collaboration XIX (2014). The error bars plotted in the panel correspond to the 143 GHz only, as the level of the corresponding uncertainties for the other frequencies is similar.

Therefore, these analyses performed in this section confirm that, as expected, the *Planck* 2015 temperature data also exhibit an anomalous signal that can be associated to the GR08 catalogue.

4.3. Polarization analysis

One of the most attractive novelties of this release is the possibility of exploring the counterpart in polarization of these temperature anomalies. Our motivation here is the following: if the $4\,\sigma$ signal measured in temperature is dominated by the primordial part of the CMB, it is reasonable to assume that it will have some form of counterpart in polarization (although it might not be detectable among the total polarization signal). Conversely, if these temperature deviations are created as a result of the presence of large clusters and voids, then no correlated signal is expected in polarization.

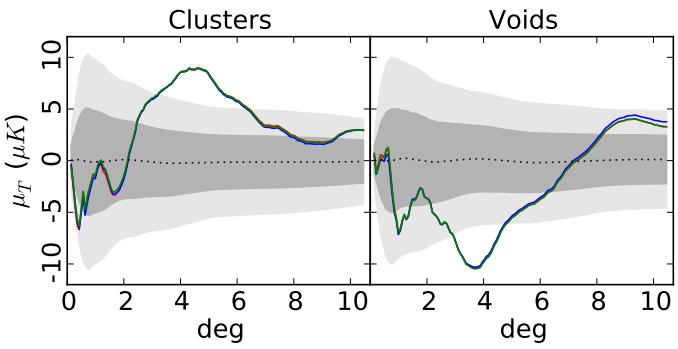

Fig. 13. Mean photometry profiles of the stacked temperature patches at the superclusters (first panel) and supervoids (second panel) positions of the GR08 catalogue. The CMB data used are the 100 GHz (red), 143 GHz (blue) and 217 GHz (green) cleaned maps supplied by SEVEM. The dotted black line and shaded regions show the mean, 1σ and 2σ error bars of the "null" profiles, i.e. computed at the same locations as the real superstructures but in 1000 FFP8 simulations processed through the 143 GHz SEVEM pipeline.

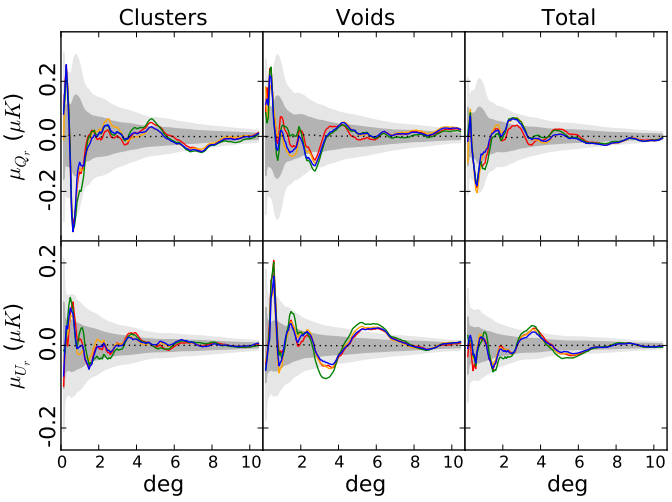

Fig. 14. Mean photometry profiles of the Q_r (first row) and U_r (second row) components stacked at the 50 superclusters (first column) and the 50 supervoids (second column) positions of GR08. The CMB maps used are supplied by COMMANDER (red), NILC (orange), SEVEM (green) and SMICA (blue). The third column shows the difference between the superclusters and the supervoids profiles. The dotted black lines show the mean value of our estimator computed with 1000 FFP8 simulations processed through the SEVEM pipeline at the same locations as the real superstructures. Shaded regions show the 1σ and 2σ error bars of these "null" profiles. Those computed for the rest of component separation methods reach a similar level.

In the following, we take several approaches in order to make the most of the potentially discriminant power of the polarization data, focusing on the study of the GR08 results. It should be noted however that the strength of these tests could be diminished by the high-pass filtering of the *Planck* 2015 polarization data release.

4.3.1. Q_r/U_r profiles significance estimation

Since the Q_r signal is proportional to the correlation between temperature and E-mode polarization (e.g., Komatsu et al. 2011), it represents a valuable observable for studying a potential polarization counterpart to the previously observed temperature signal. It should be noted that, a priori, no signal is expected in the U_r map since it would depend on temperature/B-modes correlations which are null in the standard model.

The aperture photometry profiles are shown in Fig. 14 and overall do not present any significant signal at large angular scales (greater than 1 degree). A notable exception comes from the U_r photometry profile for the voids, which does show two significant excesses around 3 and 6 degrees. However, as no T-B correlations are expected neither for the primordial CMB nor for the ISW effect, these features are most likely caused either by a fortuitous signal, and/or systematics in the polarization map that remain to be characterised – which is not in the scope of this paper. The deviations seen at angular scales below 1 degree, specially in the superclusters case, are somewhat reminiscent of the expected primordial Q_r peaks which appear due to the dynamics of the photon flows around over-density and under-density regions at the last scattering surface (i.e., hot and cold spots in the primordial CMB, see, for instance Komatsu et al. 2011; Planck Collaboration XVI 2015, for a description of these dynamics). However, this similarity is most likely fortuitous as the shape of the temperature profiles does not bear similarity to the one obtained from the stacking of the extrema of the primordial CMB. In addition, the GR08 positions do not appear to correspond with the positions of CMB extrema. The total polarization photometry profiles, computed as the differences between clusters and voids, are shown in the third column of Fig. 14.

We should however note that the significance and interpretation of these results are tricky due to the use of high-pass filtering in the polarization data, which could mitigates the signal, in principle, at all the scales of the profiles (as they include contributions from a large range of multipoles).

4.3.2. Covariance analysis

We have also tried a different, more general approach to the problem by focusing on the following question: what should we expect in the Q_r/U_r stacking signal, if the GR08 temperature signal were originated purely from primordial anisotropies?

To answer this question, we perform a set of 100,000 simulations of CMB T, Q and U maps, using the *Planck* best-fit cosmological model as input. For each one of these sets of maps, we derive the T, Q_r, and U_r stacked images corresponding to the 50 sky positions of the 50 voids of the GR08 catalogue (in order to keep the same, potentially relevant, configuration of positions in the sky). For these images, we derive the radial and photometry profiles, and end up with a collection of 2 (temperature and photometry) $\times 3$ (T, Q_r, U_r) $\times$ 100,000 profiles. More precisely, for each one of the 100,000 sets of CMB T, Q and U maps, we can construct the corresponding vector in which we put end to end the three radial profiles (of the T, Q_r, U_r stacked images) and the three photometry profiles. Using these 100,000 vectors, we construct a covariance matrix M_{ij}, which contain the covariance between any combination of angular scales of any of the $T/Q_r/U_r$ profiles. We also derive the correlation matrix N_{ij}, defined as : $N_{ij} = M_{ij}/\sqrt{M_{ii}M_{jj}}$.

In the resulting matrices, we look for the existence of significant correlations between a temperature signal with features similar to the GR08 one (i.e. peaking around a scale of 4°) and a polarization signal at any scale. The idea here is that in the simulated maps and associated stacked images that we use here, we can be certain that any stacked signal that arises in temperature is fortuitous and due to primordial anisotropies. Starting from this point, the covariance analysis allows us to get a general picture of how a primordial stacked signal in temperature is correlated to its (potential) polarization counterpart. This provides us with valuable insight when trying to test the hypothesis that the GR08 signal is purely (or partially) primordial.

After performing this analysis, the covariance/correlation matrices obtained show that the temperature photometry at $\sim 4°$ is indeed correlated with a polarization signal, both in the Q_r radial and photometry profiles (with a maximum correlation around 4° for both). The existence of these correlations is quite robust thanks to the large number of simulations, and confirm that if a significant, primordial CMB signal appears in temperature, it will have a counterpart in polarization. However, it shows that for a GR08-like signal only due to primordial CMB, the biggest correlation factors with polarization are only below $\sim 15\%$. Therefore a $3\,\sigma$ signal in temperature would only translate on average into a $\sim 0.45\,\sigma$ signal in Q_r, making it effectively impossible to detect among the rest of the polarization signal.

4.3.3. T_{E-c} and T_{E-u} maps

An alternative to the use of the Q_r and U_r components is to perform the stacking at the locations of the GR08 structures, but using the E-correlated and E-uncorrelated temperature maps of the CMB described earlier in this article (see Sect .2.1). If we were to find that most of the GR08 signal is contained in the stacked image associated with the E-correlated temperature map, this would be a strong argument towards a primordial nature for this signal. Conversely, if it is found mostly in the E-uncorrelated temperature stacked image, it would give credence to the iSW signal hypothesis. This analysis requires the E-correlated/uncorrelated temperature maps to be very reliable, and will also benefit from the use of simulations.

In Fig. 15, we show the mean photometry profiles computed from the two aforementioned maps. It appears quite clearly that for both the superclusters and the supervoids, most of the signal originally observed in temperature is contained in the E-uncorrelated map, thus apparently strengthening the hypothesis of the ISW nature of the signal, although we have to bear in mind that, by construction, the T_{E-u} map contains more power than the T_{E-c} map. Let us remark that, although the polarization data have been high-pass filtered, most of the relevant scales responsible of the anomalous temperature signal could be still present in the analyzed maps, since we have checked that the photometry profiles on high-pass filtered temperature data are very similar to those plotted in Fig. 12. On the other hand, the E-correlated part of the signal appears to sit within the expected values from simulations.

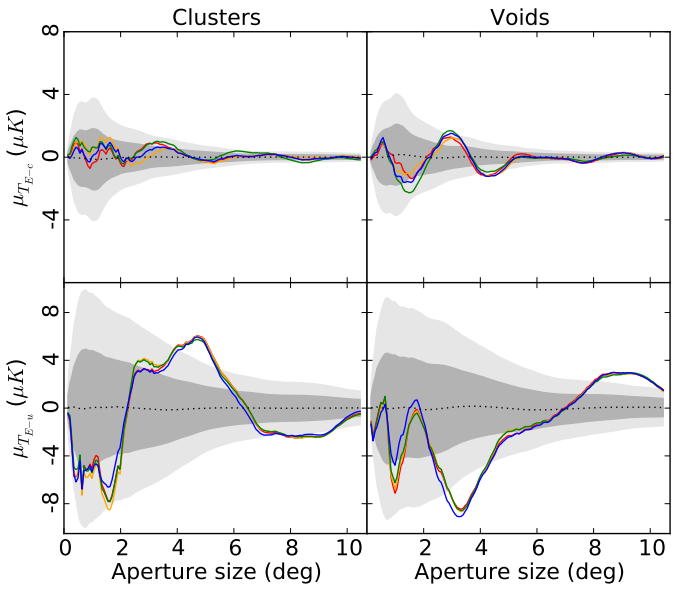

Fig. 15. Mean photometry profiles of the images for the 50 superclusters (first column) and the 50 supervoids (second column) positions of GR08, when stacking in the T_{E-c} (first row) and T_{E-u} (second row) maps computed from the CMB maps supplied by `COMMANDER` (red), `NILC` (orange), `SEVEM` (green) and `SMICA` (blue). The dotted black line represents the null hypothesis computed as the mean value of the photometry profile at 50 random positions in 1000 FFP8 simulations processed through the `SEVEM` pipeline, according the noise properties of the CMB data at the GR08 superstructures locations. The shaded regions show the 1σ and 2σ error bars of these profiles, computed as the dispersion of the mean photometry profiles of the simulations. The corresponding error bars for the different component separation methods reach a similar level.

4.4. *Planck* lensing convergence map

Another physical observable explored in the present analysis is the *Planck* lensing convergence map. As explained in Section 2.2, the Kappa map is proportional to the gravitational field and is therefore expected to be correlated with the distribution of the large-scale structures, as well as the individual objects that generate the ISW signal in the CMB. Although intricate projection (and possibly cancellation) effects are expected to be involved here, we can expect that the stacking of the lensing map at the locations of the GR08 structures will give a significant signal with respect to the null hypothesis. On the other hand, an absence of signal could indicate a problem with the structures: it could put into question the method and data used to identify them in the SDSS and therefore even question their existence, or at the very least their reported properties (size, redshift, etc). The legitimacy of such question is reinforced by recent works in the literature (see Kovács & Granett 2015) that failed to detect some of the GR08 structures in newer SDSS dataset that cover the same survey volume.

The photometry profiles computed from the Kappa map at the positions of the GR08 structures are shown in Fig. 16. The error bars are estimated with simulations generated according to the lensing model. We should be cautious here when drawing any conclusions, as the lensing map is known to be very noisy. However, it should be noted that the photometry profiles for the clusters and voids present some relatively significant features, with opposite signs, as expected if these profiles resulted from the averaging of several gravitational wells and hills respectively. The significance of these features reaches as high as $3\,\sigma$ for the voids profiles, although it is hard to pinpoint any typical scale for any of the two cases. However, the fact that the profiles tend

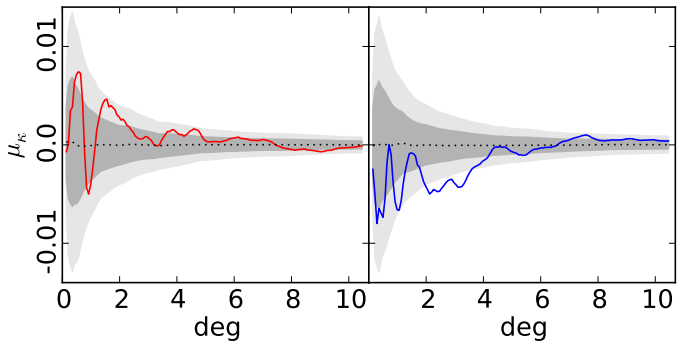

Fig. 16. Mean photometry profile of the stacked images from the *Planck* convergence lensing map, at the locations of the 50 superclusters (left panel) and the 50 supervoids (right panel) from the GR08 catalogue. The dotted black line represents the null hypothesis computed as the mean value of the photometry profiles at the corresponding GR08 positions in 1000 simulations according to the lensing model. The shaded regions show the 1σ and 2σ error bars of these profiles, computed as the dispersion of the mean photometry profiles of the simulations.

to be positive in the case of clusters and negative for voids could be pointing out in favour of the ISW interpretation of the temperature signal observed.

4.5. Summary

A stacking analysis of the GR08 positions reveals, as in Planck Collaboration XIX (2014), a temperature signature which according to the literature compares poorly with the ISW predictions. The major deviation appears about 4.5° for clusters and 3.5° for voids. An analysis of different clean frequency maps that SEVEM provides shows that the photometry profiles are not frequency dependent. This is both compatible with a pure CMB component or an ISW signal, and effectively rules out for instance a hypothetical foreground contribution.

The use of polarization as a discriminant is the main novelty of this analysis with respect to the previous *Planck* results. However, the large-scale information of *Planck* 2015 polarization is suppressed with a high-pass filtering, and the conclusions derived from these data should be therefore taken with some caution. The Q_r photometry profile is revealed to be mostly compatible with the expected signal from random positions. The absence of a counterpart in polarization is expected for a contribution caused by a secondary anisotropy. On the other hand, a theoretical covariance analysis shows that a primary temperature anisotropy does have a counterpart in polarization, but at such a weak level that it would be difficult to detect.

The analysis of the E-correlated and E-uncorrelated temperature maps at the GR08 locations supplies a complementary, and supposedly cleaner way to access the potential polarization counterpart. We found that the largest part of the temperature excess appears in the E-uncorrelated component, and is comparable to the signal recovered from a high-pass filtered version of the total temperature map. Moreover, the stacking of the E-correlated maps seems compatible with the contribution of random positions. Although we cannot conclude that the excess is not present in the primordial contribution, we do assert that is compatible with a contribution caused by a secondary anisotropy, and therefore with an ISW signal.

In addition, the stacking of the same positions on the Kappa map reveals a systematic trend in the photometry profiles to be positive for clusters and negative for voids, as expected from the evolution of gravitational wells and hills, respectively, during the dark-energy-dominated era. This appears to provide complementary evidence for the ISW hypothesis of the GR08 signal.

5. ISW map recovery

Two different approaches are followed in this work. On the one hand, as we did in Planck Collaboration XIX (2014), we apply the Linear Covariance-Based (LCB) filter firstly introduced by Barreiro et al. (2008), and recently extended in Manzotti & Dodelson (2014); Bonavera et al. (2015) to deal with several LSS tracers jointly. On the other hand, we apply a simplified version of the method proposed by Kitaura et al. (2010); Jasche & Kitaura (2010), who estimated the 3D gravitational potential out of a galaxy network given in terms of a redshift catalogue.

5.1. LCB filter

This method is able to combine all the information encoded in the CMB and LSS data about the ISW effect, in order to recover an actual map of this weak signal. In particular, the LCB filter (Barreiro et al. 2008, 2013) was originally developed to recover the ISW map by combining CMB intensity data and one LSS tracer. The method has now been extended to deal with any number of LSS surveys (Manzotti & Dodelson 2014), as well as to include polarization information (Bonavera et al. 2015) .

5.1.1. Methodology

We briefly describe here the formalism of the extended method which will be used in this paper. In order to construct the filter for n given surveys, the covariance matrix $\mathbf{C}(\ell)$ between ISW and LSS data is assumed to be known. Note that, at each multipole, $\mathbf{C}$ is a square matrix of order $t = n + 1$. To simplify the notation, the matrix is written such that the first n elements (whose harmonic coefficients are given by $g_{j=1,n}(\ell, m)$) refer to the auto- and cross-spectra involving only the n LSS tracers, while the $n+1$ element contains the auto and cross-spectra that include the ISW ($d(\ell, m)$ being the harmonic coefficients of the CMB intensity map). Through a Cholesky decomposition of the covariance matrix, we construct the matrix $\mathbf{L}$ satisfying $\mathbf{C}(\ell) = \mathbf{L}(\ell)\mathbf{L}^T(\ell)$. The estimated ISW map $\hat{s}(\ell, m)$ at each harmonic mode is then given by:

$$\hat{s}(\ell,m) = \sum_{i=1}^{n}\left[L_{it}\left(\sum_{j=1}^{n}\left(L^{-1}\right)_{ij} g_j(\ell,m)\right)\right] + \frac{L_{tt}^2}{L_{tt}^2 + C_\ell^n} \left\{d(\ell,m) - \sum_{i=1}^{n}\left[L_{it}\left(\sum_{j=1}^{n}\left(L^{-1}\right)_{ij} g_j(\ell,m)\right)\right]\right\} \quad (23)$$

where C_ℓ^n corresponds to the power spectrum of the CMB signal, without including the ISW contribution. To simplify the notation, we have dropped the dependence of the Cholesky matrix L on ℓ. Note also that although, in principle, the inversion of L should be performed only on the $n \times n$ submatrix, it is equivalent to use the full matrix, since this is triangular.

In the realistic case of incomplete sky coverage or the presence of Poissonian noise in the surveys, this can be accommodated in the previous equation. In particular, the contribution of the Poissonian noise is simply added to the auto-spectrum of

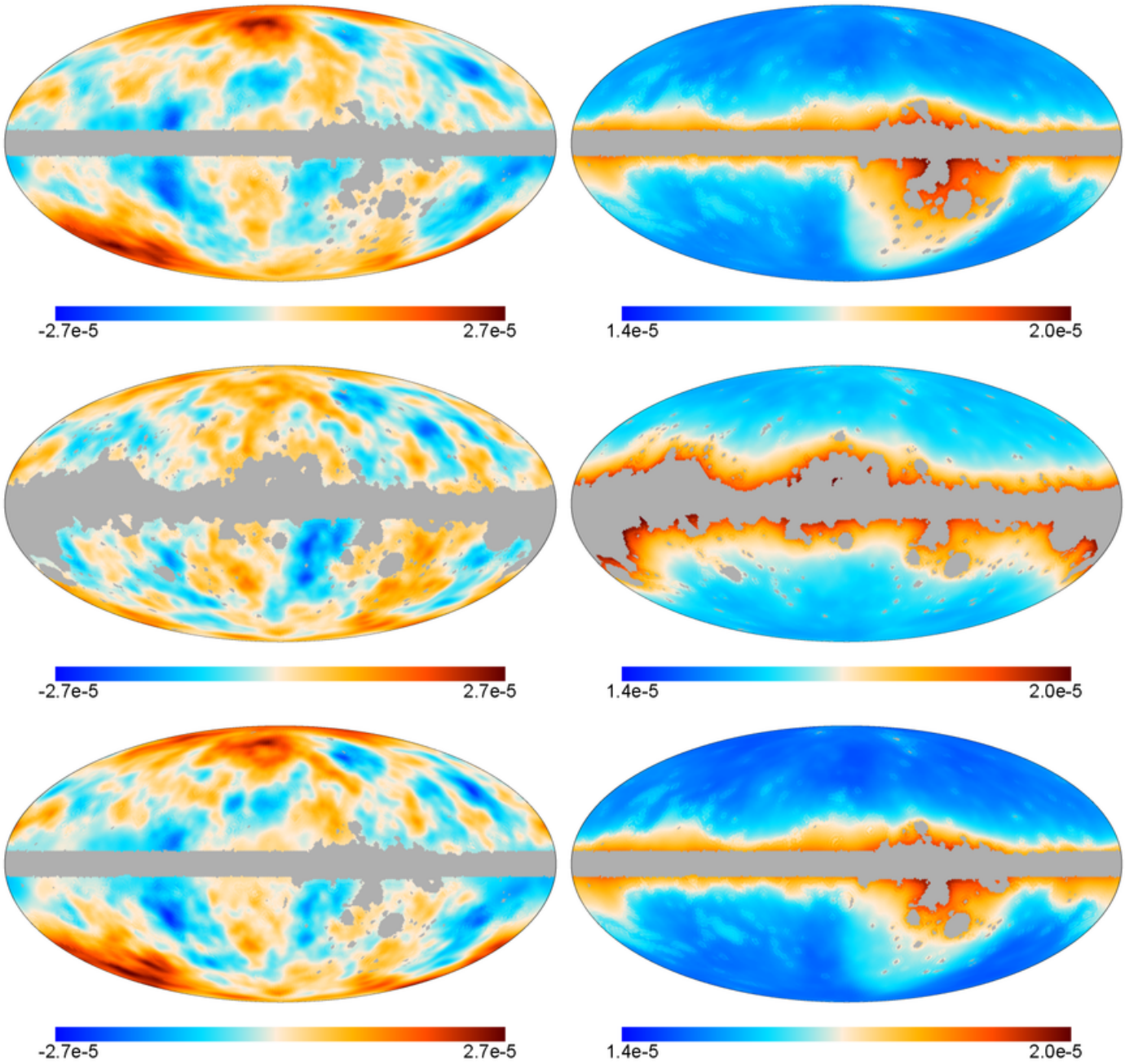

Fig. 17. Map of the recovered ISW anisotropies (left column) and the corresponding estimated error per pixel (right column) obtained from the combination of the *Planck* SEVEM CMB map with: the NVSS survey (top), the *Planck* lensing map (middle), and both tracers jointly (bottom). Units are in Kelvin.

the corresponding survey. For those data with partial sky coverage, their corresponding cross- and auto- spectra are replaced in the filter by its *masked* version, i.e., correlations among different multipoles in the power spectra are integrated with the MASTER algorithm.

5.1.2. Results

We have applied the LCB filter to the *Planck* CMB temperature map and to different combinations of the surveys described in Section 2.2. Before applying the filter, the different data sets have been masked using an apodized version of the masks shown in Sect. 2. The apodization of the masks is performed to reduce the spurious correlations introduced in the harmonic domain due to incomplete sky coverage. To construct the covariance matrix, we have made use of the models described in Sect. 2.3. The different auto- and cross- spectra are then transformed to their *masked* versions with couplings computed by the MASTER algorithm. As in previous sections, when using the Kappa and WISE maps, a cut in the lowest multipoles is imposed, meaning that these surveys do not contribute to the recovered ISW signal for $\ell < 8$ (for Kappa) and for $\ell < 9$ (for WISE). For the CMB intensity map, we consider the *Planck* SEVEM clean CMB map but similar results are expected for the other component separation methods.

To study the contribution of each data set to the final ISW map, we have applied the LCB filter to a total of seven differ-

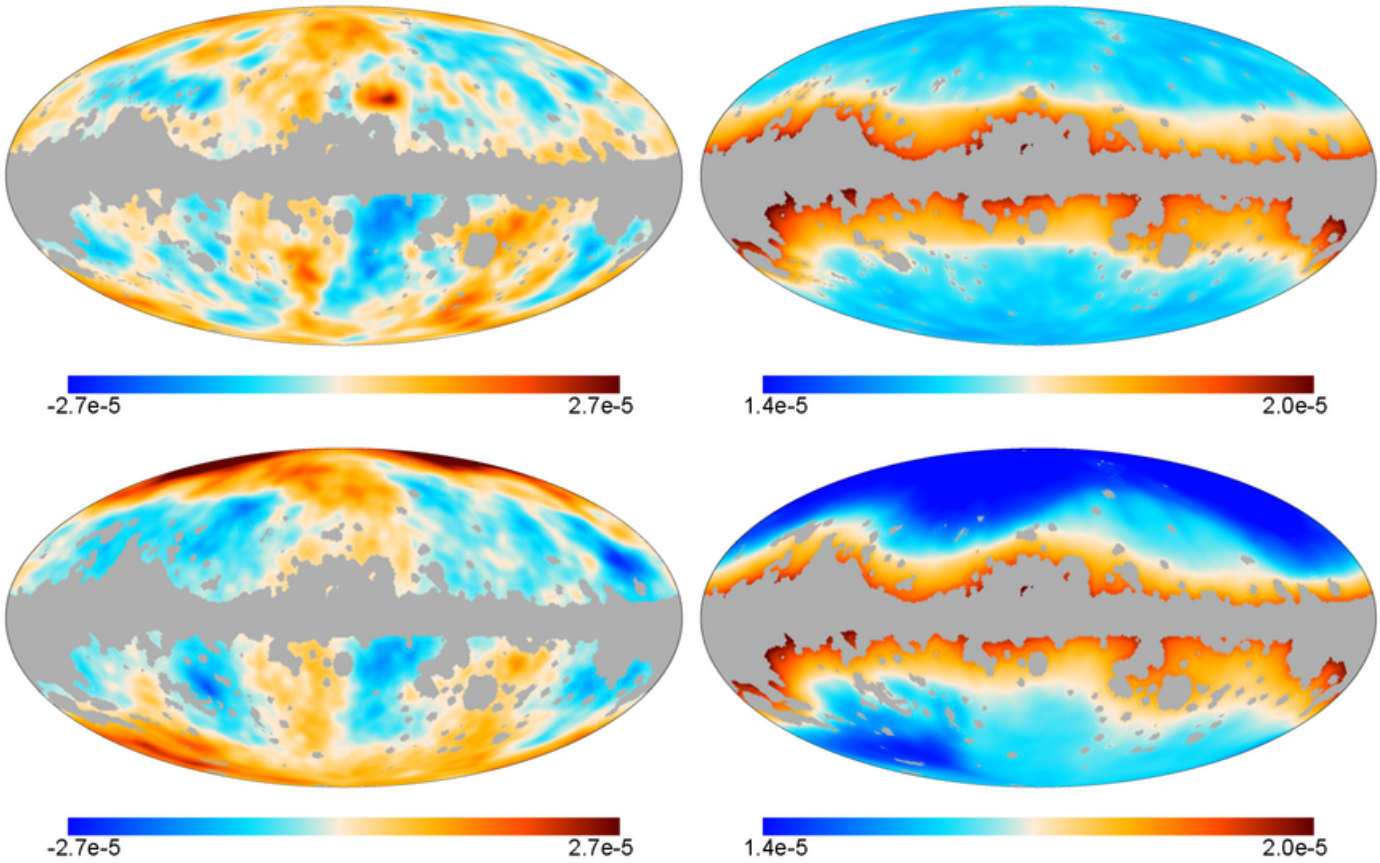

Fig. 18. Map of the recovered ISW anisotropies (left column) and the corresponding estimated error per pixel (right column) from the combination of the *Planck* SEVEM CMB map with: the two WISE surveys (top), and the two SDSS tracers (bottom). Units are in Kelvin.

ent combinations of maps. For each of these combinations, we will consider two different types of masks to study the quality of the recovered map: the intersection and the union mask. The intersection mask only excludes those pixels which are masked by all the considered data sets, since the method will reconstruct the ISW signal providing there is at least one data map available for a given position in the sky, although, as one would expect the reconstruction error would depend on the number of observations available at each pixel. Conversely, the union mask only keeps those pixels which are allowed by all the individual masks and, therefore, the reconstruction error will be more uniform in the considered region of the sky, since the same information is available for all pixels. Note that these masks represent two extreme cases and they are only used to study the quality of the reconstruction. To obtain the recovered CMB map, all data sets are used after applying its own individual mask. The different combinations used to recover the ISW map are given in Table 3, together with the sky fraction allowed by the corresponding intersection and union masks.

Fig. 17 shows the reconstruction attained by combining the CMB with NVSS, with Kappa and with both surveys simultaneously as well as their corresponding errors per pixel. The intersection mask has been applied in each case. The errors are obtained as the average dispersion of the input minus the reconstructed ISW obtained from 10 000 coherent simulations of the different data sets. The first two cases (CMB plus NVSS and CMB plus Kappa) were already given in the *Planck* 2013 paper, finding very similar results to the ones presented here. As one would expect, using both tracers jointly with the CMB (bottom row) improves the results with respect to the cases where only one tracer is used, although the improvement obtained by adding the Kappa map is only moderate. This is due, at least in part, to the low cut imposed in this tracer, which implies that the lowest multipoles are recovered using only the CMB. The quality of the ISW reconstruction can be further quantified by calculating the correlation ρ between the input s and reconstructed $\hat{s}$ maps using simulations. Before calculating the correlation, the monopole and dipole are subtracted from the input and recon-

Table 3. Mean correlation between the input and reconstructed ISW maps for different combinations of data sets.

	Intersection mask		Union mask	
	f_{sky}	$\bar{\rho}$	f_{sky}	$\bar{\rho}$
CMB and NVSS	0.84	0.56	0.56	0.58
CMB and Kappa	0.73	0.50	0.61	0.51
CMB, NVSS and Kappa	0.85	0.58	0.51	0.61
CMB and WISE	0.70	0.48	0.42	0.49
CMB and SDSS	0.69	0.53	0.19	0.60
CMB and all surveys	0.85	0.60	0.16	0.67
All surveys	0.83	0.49	0.17	0.61

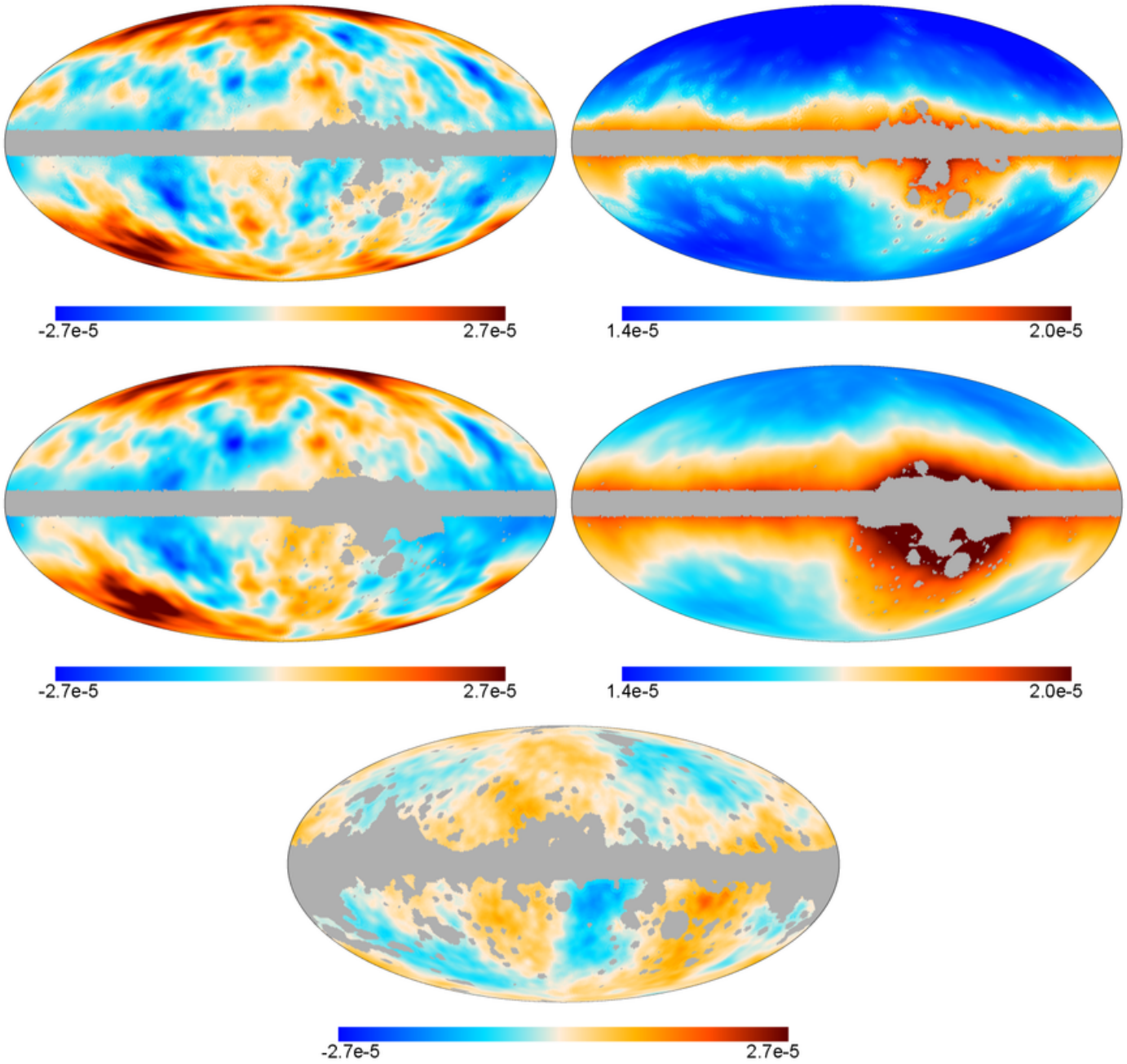

Fig. 19. The first two rows show the maps of the recovered ISW anisotropies (left column) and the corresponding estimated error per pixel (right column) from the combination of the *Planck* SEVEM CMB map and all the surveys (NVSS, WISE-AGN, WISE-GAL, SDSS-CMASS/LOWZ, SDSS-MphG, and Kappa; top), and only considering the information from these LSS tracers surveys (middle). The bottom panel gives the difference between both reconstructions, with the CMB intensity mask applied. Units are in Kelvin.

structed maps outside the considered mask. Table 3 gives the average correlation obtained over 10 000 simulations (outside the union and intersection masks) estimated for each simulation as:

$$\rho = \frac{\sum_i \omega_i (s_i - \mu_s)(\hat{s}_i - \mu_{\hat{s}})}{\sigma_s \sigma_{\hat{s}}}, \quad (24)$$

$$\omega_i = \frac{1/\sigma_i^2}{\sum 1/\sigma_i^2}.$$

where the sum runs over all the pixels allowed by the considered mask and the weights at each pixel ω_i have been estimated from the error map σ_i shown in the right column of Fig. 17. σ_s and $\sigma_{\hat{s}}$ are the dispersion of the input and reconstructed map for each simulation obtained with the same weights, while μ_s and $\mu_{\hat{s}}$ correspond to the weighted mean values of the same maps. For the union mask, an average correlation coefficient of 0.61 is found when NVSS, Kappa and the CMB are combined, to be compared to the cases when only one tracer is used: 0.58 and 0.51 for NVSS and Kappa, respectively.

Fig. 18 gives the ISW reconstructed from CMB and the WISE surveys (top) and from CMB and the SDSS surveys (bottom) as well as their corresponding errors. A bright red area is seen in the northern Galactic region, just above the central part

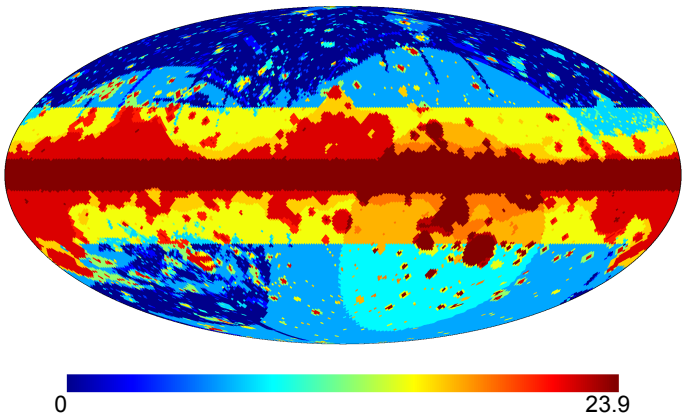

Fig. 20. Regions defined by the different intersections of the masks considered for the recovery of the ISW signal, using the LCB filter. To produce this figure, for each mask we construct a map with a constant value given by $\sqrt{k_m}$ in the excluded pixels and zero otherwise. These maps are then added together, producing the pattern seen in the figure. In particular, we choose $k_m = \{2, 4, 8, 16, 32, 64\}$ corresponding to the masks used for Kappa, NVSS, SDSS-CMASS/LOWZ, SDSS-MphG, CMB and WISE, respectively (the square root function is introduced to allow for a better visualization).

of the mask, which can be identified with systematics present in the WISE catalogues (see Fig. 4). Due to the cut at low multipoles imposed in these surveys, the structure at the largest scales is suppressed in the reconstruction, what is reflected in a larger error. The correlation between input and reconstruction outside the union mask is 0.49, the lowest value found among all the considered cases (see Table 3). Regarding the reconstruction using CMB and the SDSS surveys (bottom), we find a large signal in the relatively small regions observed by these surveys. This is refelcted in a mean correlation between input and reconstruction of 0.60 in the region allowed by the common mask, showing that the SDSS provides a sensitive tracer of the ISW.

The top row of Fig. 19 shows the reconstructed ISW signal, as well as the estimated error, obtained from the CMB map together with the six mentioned surveys (NVSS, Kappa, the two WISE and the two SDSS surveys). As one would expect, by combining all the available information, we obtain the best ISW map, with a reconstruction error of around 14 μK and a mean correlation coefficient of 0.67 outside the union mask. This corresponds to a maximum S/N ratio greater than two in certain regions of the sky. If the intersection mask is considered, the correlation coefficient is 0.60 obtained over 85 per cent of the sky. Finally, the last case (middle row) gives the ISW map reconstructed using only the six surveys, without including the CMB, which corresponds to the first term of Eq. 23. It is apparent that removing the CMB degrades the reconstruction, especially in those areas where less surveys are available, what decreases the correlation coefficient to 0.60 (union mask). To show the contribution given by the CMB to the recovery of the ISW map, the difference between these two reconstructions is also given in the bottom panel of the figure. The intensity CMB mask has been applied and the monopole and dipole removed outside this mask. Note that, as expected, the structure of this map mainly reflects that of the large scales of the intensity CMB data given in Fig. 1.

It is interesting to point out that some common structures are visible along the different reconstructions, although the maps are not expected to look exactly the same since each survey traces the ISW effect in a different way and, thus, each considered LSS tracer provides a partial reconstruction of the ISW signal.

As already mentioned, the structure of the error maps given in the right columns of Figs. 17, 18 and 19 reflects the different sky coverages of the considered surveys, showing the contribution of each data set to the final ISW reconstruction. This can be further explored by comparing these different structures with Fig. 20, which shows the intersection regions defined by the CMB and surveys masks. Each colour corresponds to a region where the intersection of a different sets of masks occurs, being the dark blue area observed by all data sets whereas the dark red region gives those pixels which are not observed by any of the data sets.

5.2. Construction of an ISW map from 3D galaxy surveys

A different approach consists in using redshift information in galaxy catalogues to provide a full 3D gravitational potential reconstruction, which, under the assumption of a given cosmological framework, can be trivially extended into an ISW map estimate, for linearly evolving structures. We remark that in this case very high redshift precision is not required, since the gravitational potential sourcing the ISW is coming from large scales (at or above $100\,h^{-1}$ Mpc typically), leaving room for redshift uncertainties at the level of $\Delta z \sim 0.01$–0.03. On such large scales, redshift space distortions can be safely ignored.

5.2.1. Methodology

The procedure must invert a galaxy density field into a potential field in a given region of the universe that is limited by the selection function of the survey and the sky mask. This is done by applying the Poisson equation in Fourier space, and expressing the gravitational potential in terms of the density contrast, namely:

$$-k^2\Phi_{\boldsymbol{k}} = \frac{3}{2}H_0^2\Omega_{\rm m}a^{-1}(z)\delta_{\boldsymbol{k}}. \quad (25)$$

In this equation, $\Phi_{\boldsymbol{k}}$ stands for the Fourier transform of the gravitational potential, $\Omega_{\rm m}$ denotes the total matter density parameter and H_0 corresponds to the Hubble constant. The factor $a^{-1}(z) = 1 + z$ corresponds to the inverse of the cosmological scale factor, and $\delta_{\boldsymbol{k}}$ is the (time dependent) matter density contrast Fourier transform for the mode $\boldsymbol{k}$, as estimated from the galaxy density. The time dependence of the gravitational potentials is thus given by these last two quantities. The use of the Poisson equation is justified since we are considering scales that, despite being larger than typical density clustering lengths, are well inside the horizon. When handling the equation above, the presence of an effective volume mask (induced either by the sky mask and/or the survey selection function) may introduce biases in our gravitational potential estimates. In order to handle this, we choose to conduct our particular *Poissonian data augmentation*, consisting in the following steps:

– We place the galaxies in a regular 3D grid in comoving coordinates. For that we use the central value of the redshift assigned to each source. As it will be shown below, we find that, when accounting for all other sources of uncertainty, the level of uncertainty associated to errors in the photometric redshifts is sub-dominant and thus it can be neglected at first order.

– In those grid cells excluded by the sky mask, we introduce a number of mock galaxies that is driven from a Poissonian realisation with an average galaxy number density equal to the average number density of cells at the same distance but not excluded by the sky mask.
– In all grid cells, we introduce another set of randomly, Poisson distributed mock galaxies in order to make the selection function constant with respect to depth/redshift.

We assume that the selection function of the survey and the sky mask can be factorized separately, in such a way that the selection function depends exclusively on the depth/redshift. In practice, this may not be the case for regions with high extinction, but we assume that most of these regions should be discarded by the sky mask of the survey.

This procedure should provide a homogenized galaxy density field in the entire 3D grid, which can be inverted into a gravitational potential field. By conducting a set of simulations for each of the stages of our Poissonian data augmentation approach, it is possible to assess the dependence of the resulting gravitational potential field on each step. This potential reconstruction method is a very simplified version of more sophisticated approaches of inversion of observed galaxy surveys (e.g., Kitaura et al. 2010; Jasche & Kitaura 2010, to cite two pioneering works).

Finally, the gravitational potential time derivative is obtained from the 3D gravitational potential after imposing that follows the linear theory predictions of the reference cosmological model. That is, we express the derivative of the gravitational potential field with respect to that radial comoving distance η following this equation:

$$\frac{d\Phi_{\boldsymbol{k}}}{d\eta} = \frac{3}{2}H(z)H_0^2\Omega_{\rm m}\left[1+\frac{d\log D_\delta}{d\log(1+z)}\right]\frac{\delta_{\boldsymbol{k}}}{k^2}$$
$$= -\Phi_{\boldsymbol{k}}\,H(z)a(z)\left[1+\frac{d\log D_\delta}{d\log(1+z)}\right]. \qquad (26)$$

In this equation, $H(z)$ denotes the Hubble parameter, H_0 its current value, and $D_\delta(z)$ the redshift dependent linear growth factor of the density perturbations. The final ISW map is obtained after integrating the $d\Phi_{\boldsymbol{k}}/d\eta$ 3D grid along the line of sight.

5.2.2. Results

In this section we present the results of inverting the 2MPZ survey into a gravitational potential field whose time derivative is then projected along the line of sight.

We place the galaxies of this survey in a 3D grid of 128^3 cells of $6\,h^{-1}$ Mpc on a side, centred upon the observer. This means that the maximum redshift considered is $z_{\rm max} \simeq 0.13$, and that more than 85 % of the 2MPZ sources are actually placed inside the grid. This choice of $z_{\rm max}$ is motivated as a compromise between sampling a large cosmological volume and having a representative amount of galaxies tracing the potential wells: increasing $z_{\rm max}$ degrades potential reconstructions at large distances from the observer and provides little information about the ISW.

Provided that the ISW is generated out to redshifts $z \sim 1$, our choice of $z_{\rm max}$ should contain a small fraction of the total ISW generated in our visible universe. Nevertheless the contribution of this relatively nearby cosmological volume to the low multipole anisotropy power has been claimed not to be completely negligible, and it has been argued that it may be of relevance in the context of the CMB large angle anomalies (e.g., Francis & Peacock 2010; Rassat et al. 2013).

When conducting the reconstruction, we impose a sky mask for all pixels with $|b_{\rm gal}| < 10°$ for which the Galaxy heavily impacts the selection function of the survey. The result of the inversion of the galaxy density field into the gravitational potential field and its time derivative is shown in Fig. 21. The recovered ISW map resembles the large scale structure of the projected density map (Fig. 4): the positive structure of the ISW map traces, in the North Galactic hemisphere, the presence of well known superclusters like Ursa Major, Virgo, Centaurus or Hydra, while in the southern hemisphere, at slightly negative galactic latitudes, the most prominent negative spot corresponds to the Local Void.

We find however that the amplitude of the recovered ISW map is too small to contribute significantly to the total CMB map on the largest scales. In Fig. 22 filled black circles display the angular power spectrum of the recovered ISW from 2MPZ.

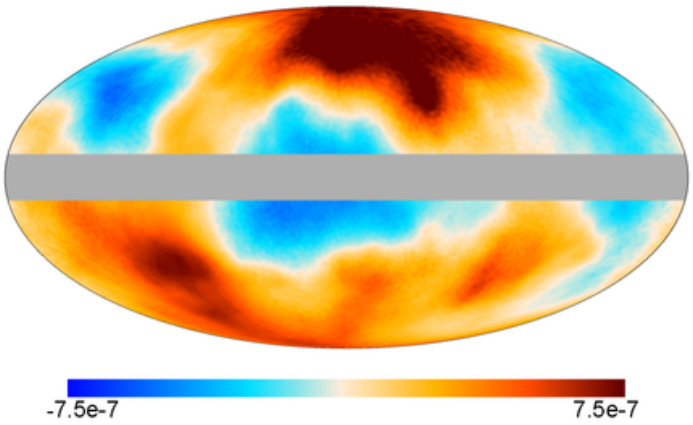

Fig. 21. Map of the recovered ISW from the 2MPZ catalogue. Units are in Kelvin.

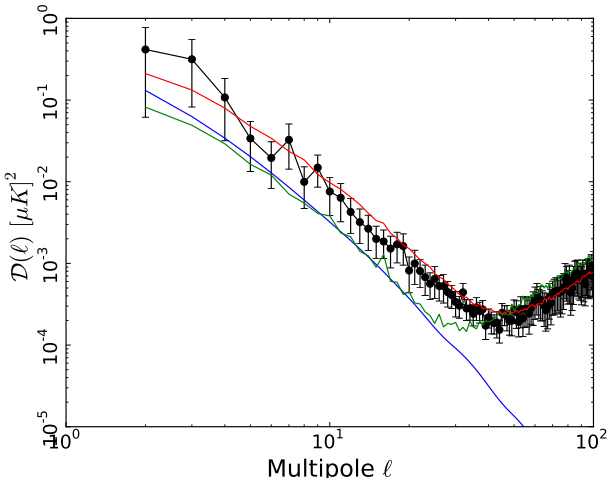

Fig. 22. Comparison of the ISW recovered angular power spectrum from 2MPZ data (black solid circles) with theoretical expectations (blue solid line) and the average of ideal (green solid line) and realistic (red solid line) simulations of our density-to-potential inversion algorithm (see text for details).

The RMS of this map is dominated by the quadrupole, whose amplitude is found to be $C_{l=2}^{\rm 2MPZ,\,ISW} = 0.44 \pm 0.37\,(\mu{\rm K})^2$, driving the RMS map to be at the level of only $0.56\,\mu$K. Thus our estimated quadrupole amplitude of the ISW map generated by 2MPZ seems to be in tension with the estimate of Rassat et al. (2013) since these authors quote a theoretical expectation for the ISW quadrupole of $12 \pm 10\,(\mu{\rm K})^2$, i.e., almost two orders of magnitude above our estimate.

We next compare the amplitude of the angular power spectrum of our recovered ISW map with theoretical expectations. For this purpose, we make use of a modified Boltzmann code that provides the ISW angular power spectrum for a generic galaxy sample that is probing the large-scale structure under the same selection function as the one estimated for 2MPZ. We remark that this estimate of the ISW amplitude is independent of the bias of the galaxy sample. Such prediction is provided by the thick blue solid line in Fig. 22. We can see that the recovered ISW power spectrum is significantly higher than this expectation. In order to understand this, we run 100 Monte Carlo simulations of Gaussian density fields in the same 3D spatial grid used for the density to potential inversion in real data. These Gaussian simulations are obtained from a ΛCDM matter power spectrum corresponding to our fiducial cosmological model at $z = 0$. In this set of MC *ideal* simulations we only impose the radial selection function of the 2MPZ survey at the time of conducting the line of sight integral of the time derivative of the gravitational potentials, but ignore all effects of radial selection function, photometric redshift errors and shot noise when producing the potential maps. The green solid line provides the average angular power spectrum obtained from this set of simulated maps. The agreement of this computation with the theoretical expectation is very good for multipoles $\ell < 20$: artifacts related to the projection of the finite grid cells on the sky introduce spurious power that becomes dominant on smaller scales.

We also run a second set of MC *realistic* simulations which are based upon the same set of Gaussian simulations just described above, but after including the impact of the 2MPZ radial selection function, photometric redshift errors and shot noise as it was required for real data. The photometric redshift errors were simulated by adding a normal deviate of RMS $\sigma_z = 0.015$ to the "correct" redshifts of the simulated galaxies. Note that in both sets of simulations the initial 3D Gaussian matter density field is identical, but in this case Poissonian augmentation was required (1) in the sky-mask excluded areas and (2) at large redshifts, in order to avoid radial galaxy density gradients associated to the radial selection function. The average angular power spectrum from this set of simulated ISW maps is displayed in Fig. 22 by the red solid line. We find in this case much better agreement with the result from the real 2MPZ catalogue. From this set of simulations we obtain the error bars for the recovered 2MPZ ISW power spectrum multipoles.

Despite of the uncertainties of the amplitude of the recovered ISW map, this analysis shows that it is highly implausible that, in a standard ΛCDM scenario, the ISW generated by the gravitational potentials hosting the 2MPZ galaxies can significantly modify the large scale pattern of the CMB: the expected quadrupole of the ISW is about three orders of magnitude below the total CMB quadrupole amplitude.

These two sets of simulations should provide a fair description of the total error budget introduced by our approach. In Fig. 23, filled red triangles display the ratio of the RMS of the recovered angular power spectrum multipoles over their average value for the realistic set of simulations. For instance, for the recovered quadrupole this plot shows that the RMS of the quadrupole amounts to roughly 90 % of its amplitude. Note that the quoted uncertainty in the recovered angular power spectrum multipoles includes the contribution from cosmic variance. For the sake of comparison, the solid blue line depicts this ratio for the case of a pure Gaussian field without any coupling between different multipoles and the same sky coverage as for 2MPZ and the Monte Carlo simulations: in this case this ratio obeys the simple form $\sqrt{2/f_{\rm sky}/(2l+1)}$. This trend is closely followed by the output of the ideal MC simulations ignoring the impact of the radial selection function and the Poissonian augmentation (green filled circles). For multipoles below $\ell = 20$ errors in the recovered angular power spectrum multipoles are close to the Gaussian prediction, but on smaller scales errors associated to the line of sight integral become dominant.

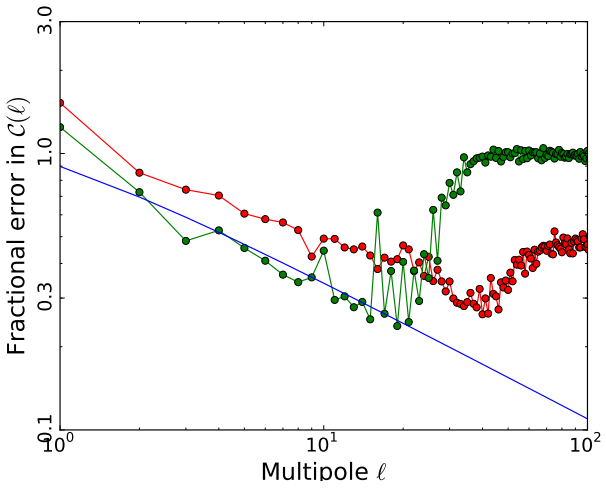

Fig. 23. Relative uncertainty in the recovered ISW angular power spectrum multipoles. Red triangles and green circles refer to the *realistic* and *ideal* sets of MC simulations, respectively.

Finally, in order to provide an estimate on how the recovered ISW maps by our technique actually resemble the real, underlying ISW maps, Fig. 24 displays the correlation coefficient between the ISW recovered map under the ideal and realistic set of simulations. This correlation coefficient is defined as $r_\ell = \langle a_{\ell,m}^{\rm real} (a_{\ell,m}^{\rm ideal})^\star \rangle / (C_\ell^{\rm real} C_\ell^{\rm ideal})^{1/2}$, that is, the ratio of the cross angular spectrum of each pair of maps over the square root of the product of the auto spectra. The correlation coefficient is, on average, about 0.8 in the multipole range $\ell \in [2, 10]$, and above 0.70 in $\ell \in [2, 20]$. On smaller angular scales there is little ISW power and spurious power deletes any ISW information in the recovered maps.

Finally, we conducted the test of performing a new realistic set of MC simulations for which the uncertainty in the radial distance to galaxies associated to photometric redshift errors is switched off. We found very little difference in the uncertainty in the recovered ISW angular power spectrum multipoles and in the correlation coefficients, suggesting that photo-z errors at the level $\sigma_z = 0.015$ are not a dominant source of uncertainty for our ISW reconstruction approach.

6. Conclusions

We presented a study of the ISW effect using the *Planck* 2015 data release, which provides higher sensitivity temperature anisotropies maps with respect to the previous *Planck* 2013 re-

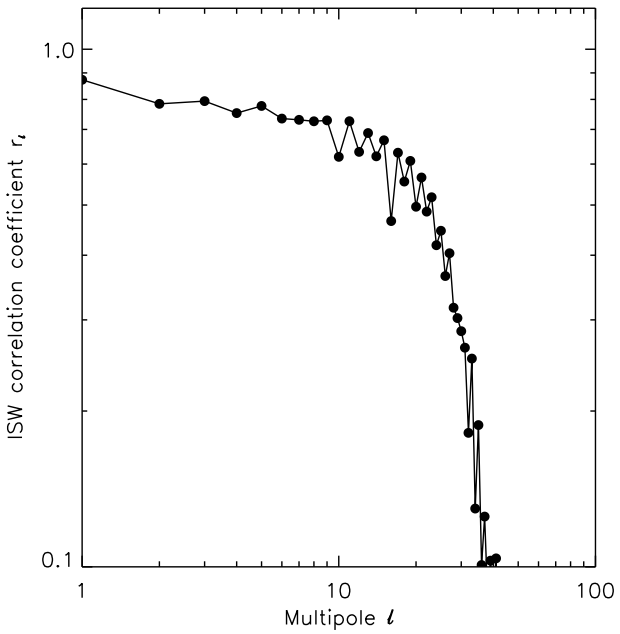

Fig. 24. Correlation coefficient between the ISW recovered maps in the realistic and ideal set of simulations.

lease, as well as CMB polarization data at angular scales below 5°. As compared to our past publication (Planck Collaboration XIX 2014), we have extended the analysis in the following manners.

First, we have included additional galaxy (WISE-GAL) and AGN (WISE-AGN) catalogues from the WISE survey as LSS tracers to be correlated with the four *Planck* CMB maps (COMMANDER, NILC, SEVEM, and SMICA). These tracers, in combination with the NVSS radio catalogue, the photometric luminous galaxy (LG) catalogue from the Baryonic Oscillation Spectroscopic Survey (BOSS) of the SDSS III (SDSS-CMASS/LOWZ), and the photometrically-selected galaxies from the SDSS-DR8 catalogue (SDSS-MphG), yield a detection of the ISW signal at $2.9\,\sigma$. This detection is dominated by the NVSS catalogue ($2.6\,\sigma$), while the combination of the two SDSS catalogues provides a $2.7\,\sigma$, and the two WISE render a $1.9\,\sigma$ signal-to-noise ratio.

Second, we have also improved the characterization of the ISW effect through the ISW-lensing bispectrum, since the higher signal-to-noise ratio of the *Planck* 2015 temperature data and the new polarization data allows us to improve the reconstruction of the *Planck* lensing signal. In particular, we increase the detection achieved in the previous release in $\approx 20\%$, reaching a $\approx 3\,\sigma$ detection. We have performed a new analysis, in which the *Planck* ISW-lensing is combined with the cross-correlation of the *Planck* CMB with all the previously mentioned LSS tracers, obtaining a total detection of the ISW effect at $4\,\sigma$. The four CMB maps provide similar detection levels for all the cross-correlation combinations.

Third, we have investigated the anomalous nature of the ISW signal detected through the stacking of the CMB anisotropies in the positions of known superstructures (Granett et al. 2008a). We have confirmed that the aperture photometry profiles around the 50 supervoids and 50 superclusters of the GR08 catalogue exhibit a maximum amplitude of $\approx -11\,\mu$K (at scales of $\approx 3.5°$) and $\approx 9\,\mu$K (at scales of $\approx 4.5°$), respectively. These amplitudes are much larger than expected in the context of the standard ΛCDM scenario. We have used the *Planck* polarization data to explore further the origin of this signal. We do not find evidence for a positive correlation of this signal in the polarization data, indicating hence that the origin of the temperature signal is, indeed, compatible with a secondary anisotropy, as expected for the ISW. These aperture photometry are very consistent for the four CMB polarization maps, as well as for the SEVEM clean frequency maps at 100, 143 and 217 GHz, which reduces very much the possibility that this signal is significantly affected by contamination from residual galactic and extragalactic foregrounds. Similar conclusions are obtained through the analysis of the E-correlated and E-uncorrelated counterparts of the temperature signal, only finding excess in the latter, as expected for the ISW effect. Finally, we have also stacked patches of the *Planck* lensing map on the locations of these superstructures, finding a positive correlation for both, cluster and voids, offering an extra evidence in favour of the ISW hypothesis.

Third, we have improved the recovery of the ISW fluctuations in the sky, by using a generalization of the a linear covariance-based filter. In particular, we have used the five galaxy catalogues mentioned above, as well as the *Planck* lensing convergence map to infer a map of the secondary anisotropies associated to the ISW caused by the LSS traced by these surveys. Using simulations, we have been able to provide an associated RMS map, with a mean value of $\approx 14\,\mu$K per pixel of $\approx 1°$. Our ISW reconstruction provides regions where the ISW fluctuations are recovered at more than $2\,\sigma$. We have also explored an alternative approach to estimate a map of ISW anisotropies, by attempting a direct inversion of the density field as traced by the 2MASS Photometric Redshift catalogue into its corresponding gravitational potential field. The typical RMS of the ISW induced by these nearby structures is, as expected, very low ($\approx 0.6\,\mu$K), and this is well below the level of the measured large angular CMB fluctuations. Nevertheless, the angular power spectrum of the ISW effect produced by these structures is well recovered for $\ell \lesssim 20$.

Therefore, the cross-correlation of the *Planck* CMB maps with different tracers of the LSS confirms the detection of the ISW effect at the expected level for the ΛCDM model. The current detection level could be improved, from the CMB side, by analysing the next *Planck* release, which will include large scale polarization data. On the other hand, the ISW estimation through the stacking of the CMB anisotropies on the locations of certain superstructures remains an open problem. Current polarization data seem to support the secondary nature of this stacked signal, although the future full polarization *Planck* data could help to probe further this hypothesis. However, it seems that the most important insights should come from the theoretical side.

Acknowledgements. The Planck Collaboration acknowledges the support of: ESA; CNES and CNRS/INSU-IN2P3-INP (France); ASI, CNR, and INAF (Italy); NASA and DoE (USA); STFC and UKSA (UK); CSIC, MINECO, JA, and RES (Spain); Tekes, AoF, and CSC (Finland); DLR and MPG (Germany); CSA (Canada); DTU Space (Denmark); SER/SSO (Switzerland); RCN (Norway); SFI (Ireland); FCT/MCTES (Portugal); ERC and PRACE (EU). A description of the Planck Collaboration and a list of its members, indicating which technical or scientific activities they have been involved in, can be found at http://www.cosmos.esa.int/web/planck/planck-collaboration. Some of the results in this paper have been derived using the HEALPix package (Górski et al. 2005). We acknowledge the computer resources, technical expertise and assistance provided by the Spanish Supercomputing Network (RES) node at Universidad de Cantabria, and the support provided by the Advanced Computing and e-Science team at IFCA. Part of this work was undertaken on the STFC COSMOS@DiRAC HPC Facilities at the University of Cambridge, funded by UK BIS NEI grants.

References

Adelman-McCarthy, J. K., Agüeros, M. A., Allam, S. S., et al., The Sixth Data Release of the Sloan Digital Sky Survey. 2008, ApJS, 175, 297, arXiv:0707.3413

Aihara, H., Allende Prieto, C., An, D., et al., The Eighth Data Release of the Sloan Digital Sky Survey: First Data from SDSS-III. 2011, ApJS, 193, 29, arXiv:1101.1559

Barreiro, R. B., Vielva, P., Hernandez-Monteagudo, C., & Martinez-Gonzalez, E., A Linear Filter to Reconstruct the ISW Effect From CMB and LSS Observations. 2008, IEEE Journal of Selected Topics in Signal Processing, 2, 747

Barreiro, R. B., Vielva, P., Marcos-Caballero, A., & Martínez-González, E., Integrated Sachs-Wolfe effect map recovery from NVSS and WMAP 7-yr data. 2013, MNRAS, 430, 259, arXiv:1208.2350

Bilicki, M., Jarrett, T. H., Peacock, J. A., Cluver, M. E., & Steward, L., Two Micron All Sky Survey Photometric Redshift Catalog: A Comprehensive Three-dimensional Census of the Whole Sky. 2014, ApJS, 210, 9, arXiv:1311.5246

Bonavera, L., Barreiro, R. B., Marcos-Caballero, A., & Vielva, P., Using large-scale structure tracers and CMB temperature and polarization anisotropies to reconstruct the ISW fluctuations. 2015, MNRAS to be submitted, arXiv:1502.xxxx

Boughn, S. & Crittenden, R., A correlation between the cosmic microwave background and large-scale structure in the Universe. 2004, Nature, 427, 45, arXiv:astro-ph/0305001

Bucher, M., van Tent, B., & Carvalho, C. S., Detecting bispectral acoustic oscillations from inflation using a new flexible estimator. 2010, MNRAS, 407, 2193, arXiv:0911.1642

Cabré, A., Fosalba, P., Gaztañaga, E., & Manera, M., Error analysis in cross-correlation of sky maps: application to the Integrated Sachs-Wolfe detection. 2007, MNRAS, 381, 1347, arXiv:astro-ph/0701393

Cai, Y.-C., Neyrinck, M. C., Szapudi, I., Cole, S., & Frenk, C. S., A Possible Cold Imprint of Voids on the Microwave Background Radiation. 2014, ApJ, 786, 110, arXiv:1301.6136

Collister, A. A. & Lahav, O., ANNz: Estimating Photometric Redshifts Using Artificial Neural Networks. 2004, PASP, 116, 345, arXiv:astro-ph/0311058

Condon, J. J., Cotton, W. D., Greisen, E. W., et al., The NRAO VLA Sky Survey. 1998, AJ, 115, 1693

Cooray, A. & Melchiorri, A., Searching for integrated Sachs Wolfe effect beyond temperature anisotropies: CMB E-mode polarization galaxy cross-correlation. 2006, Journal of Cosmology and Astro-Particle Physics, 1, 18, arXiv:astro-ph/0511054

Corasaniti, P.-S., Giannantonio, T., & Melchiorri, A., Constraining dark energy with cross-correlated CMB and large scale structure data. 2005, Phys. Rev. D, 71, 123521, arXiv:astro-ph/0504115

Crittenden, R. G. & Turok, N., Looking for a Cosmological Constant with the Rees-Sciama Effect. 1996, Physical Review Letters, 76, 575, arXiv:astro-ph/9510072

Fergusson, J. R., Liguori, M., & Shellard, E. P. S., General CMB and primordial bispectrum estimation: Mode expansion, map making, and measures of F_{NL}. 2010, Phys. Rev. D, 82, 023502, arXiv:0912.5516

Ferraro, S., Sherwin, B. D., & Spergel, D. N., A WISE measurement of the ISW effect. 2014, ArXiv e-prints, arXiv:1401.1193

Fosalba, P., Gaztañaga, E., & Castander, F. J., Detection of the Integrated Sachs-Wolfe and Sunyaev-Zeldovich Effects from the Cosmic Microwave Background-Galaxy Correlation. 2003, ApJ, 597, L89, arXiv:astro-ph/0307249

Francis, C. L. & Peacock, J. A., An estimate of the local integrated Sachs-Wolfe signal and its impact on cosmic microwave background anomalies. 2010, MNRAS, 406, 14

Frommert, M. & Enßlin, T. A., Ironing out primordial temperature fluctuations with polarization: optimal detection of cosmic structure imprints. 2009, MNRAS, 395, 1837

Frommert, M., Enßlin, T. A., & Kitaura, F. S., Optimal integrated Sachs-Wolfe detection and joint likelihood for cosmological parameter estimation. 2008, MNRAS, 391, 1315, arXiv:0807.0464

Giannantonio, T., Measuring dark energy with the integrated Sachs-Wolfe effect. 2008, ArXiv e-prints 0805.3645, arXiv:0805.3645

Giannantonio, T., Crittenden, R., Nichol, R., & Ross, A. J., The significance of the integrated Sachs-Wolfe effect revisited. 2012, MNRAS, 426, 2581, arXiv:1209.2125

Giannantonio, T., Crittenden, R. G., Nichol, R. C., et al., High redshift detection of the integrated Sachs-Wolfe effect. 2006, Phys. Rev. D, 74, 063520, arXiv:astro-ph/0607572

Giovi, F. & Baccigalupi, C. 2005, in IAU Symposium, Vol. 225, Gravitational Lensing Impact on Cosmology, ed. Y. Mellier & G. Meylan, 117–122

Giovi, F., Baccigalupi, C., & Perrotta, F., Constraining the dark energy dynamics with the cosmic microwave background bispectrum. 2003, Phys. Rev. D, 68, 123002, arXiv:astro-ph/0308118

Goldberg, D. M. & Spergel, D. N., Microwave background bispectrum. II. A probe of the low redshift universe. 1999, Phys. Rev. D, 59, 103002, arXiv:astro-ph/9811251

Górski, K. M., Hivon, E., Banday, A. J., et al., HEALPix: A Framework for High-Resolution Discretization and Fast Analysis of Data Distributed on the Sphere. 2005, ApJ, 622, 759, arXiv:astro-ph/0409513

Granett, B. R., Neyrinck, M. C., & Szapudi, I., An Imprint of Superstructures on the Microwave Background due to the Integrated Sachs-Wolfe Effect. 2008a, ApJ, 683, L99, arXiv:0805.3695

Granett, B. R., Neyrinck, M. C., & Szapudi, I., Dark Energy Detected with Supervoids and Superclusters. 2008b, ArXiv e-prints 0805.2974, arXiv:0805.2974

Hambly, N. C., MacGillivray, H. T., Read, M. A., et al., The SuperCOSMOS Sky Survey - I. Introduction and description. 2001, MNRAS, 326, 1279, arXiv:astro-ph/0108286

Hanson, D., Challinor, A., & Lewis, A., Weak lensing of the CMB. 2010, General Relativity and Gravitation, 42, 2197, arXiv:0911.0612

Hanson, D., Smith, K. M., Challinor, A., & Liguori, M., CMB lensing and primordial non-Gaussianity. 2009, Phys. Rev. D, 80, 083004, arXiv:0905.4732

Hernández-Monteagudo, C., Revisiting the WMAP-NVSS angular cross correlation. A skeptic's view. 2010, A&A, 520, A101, arXiv:0909.4294

Hernández-Monteagudo, C., Ross, A. J., Cuesta, A., et al., The SDSS-III Baryonic Oscillation Spectroscopic Survey: constraints on the integrated Sachs-Wolfe effect. 2013, MNRAS, arXiv:1303.4302

Hernández-Monteagudo, C. & Smith, R. E., On the signature of z 0.6 superclusters and voids in the Integrated Sachs-Wolfe effect. 2013, MNRAS, 435, 1094, arXiv:1212.1174

Hinshaw, G., Spergel, D. N., Verde, L., et al., First-Year Wilkinson Microwave Anisotropy Probe (WMAP) Observations: The Angular Power Spectrum. 2003, ApJS, 148, 135, arXiv:astro-ph/0302217

Hivon, E., Górski, K. M., Netterfield, C. B., et al., MASTER of the Cosmic Microwave Background Anisotropy Power Spectrum: A Fast Method for Statistical Analysis of Large and Complex Cosmic Microwave Background Data Sets. 2002, ApJ, 567, 2, arXiv:astro-ph/0105302

Ho, S., Hirata, C., Padmanabhan, N., Seljak, U., & Bahcall, N., Correlation of CMB with large-scale structure. I. Integrated Sachs-Wolfe tomography and cosmological implications. 2008, Phys. Rev. D, 78, 043519, arXiv:0801.0642

Hotchkiss, S., Nadathur, S., Gottlöber, S., et al., The Jubilee ISW Project II: observed and simulated imprints of voids and superclusters on the cosmic microwave background. 2014, ArXiv e-prints, arXiv:1405.3552

Hu, W., Weak lensing of the CMB: A harmonic approach. 2000, Phys. Rev. D, 62, 043007, arXiv:astro-ph/0001303

Hu, W., Dark synergy: Gravitational lensing and the CMB. 2002, Phys. Rev. D, 65, 023003, arXiv:astro-ph/0108090

Hu, W. & Okamoto, T., Mass Reconstruction with Cosmic Microwave Background Polarization. 2002, ApJ, 574, 566, arXiv:astro-ph/0111606

Huchra, J. P., Geller, M. J., & Corwin, Jr., H. G., The CfA Redshift Survey: Data for the NGP +36 Zone. 1995, ApJS, 99, 391

Huchra, J. P., Macri, L. M., Masters, K. L., et al., The 2MASS Redshift Survey Description and Data Release. 2012, ApJS, 199, 26, arXiv:1108.0669

Ilić, S., Langer, M., & Douspis, M., Detecting the integrated Sachs-Wolfe effect with stacked voids. 2013, A&A, 556, A51, arXiv:1301.5849

Jarrett, T. H., Chester, T., Cutri, R., et al., 2MASS Extended Source Catalog: Overview and Algorithms. 2000, AJ, 119, 2498, arXiv:astro-ph/0004318

Jasche, J. & Kitaura, F. S., Fast Hamiltonian sampling for large-scale structure inference. 2010, MNRAS, 407, 29, arXiv:0911.2496

Jones, D. H., Read, M. A., Saunders, W., et al., The 6dF Galaxy Survey: final redshift release (DR3) and southern large-scale structures. 2009, MNRAS, 399, 683, arXiv:0903.5451

Kamionkowski, M., Matter-microwave correlations in an open universe. 1996, Phys. Rev. D, 54, 4169, arXiv:astro-ph/9602150

Kamionkowski, M. & Loeb, A., Getting around cosmic variance. 1997, Phys. Rev. D, 56, 4511, arXiv:astro-ph/9703118

Kitaura, F.-S., Jasche, J., & Metcalf, R. B., Recovering the non-linear density field from the galaxy distribution with a Poisson-lognormal filter. 2010, MNRAS, 403, 589, arXiv:0911.1407

Komatsu, E., Kogut, A., Nolta, M. R., et al., First-Year Wilkinson Microwave Anisotropy Probe (WMAP) Observations: Tests of Gaussianity. 2003, ApJS, 148, 119, arXiv:astro-ph/0302223

Komatsu, E., Smith, K. M., Dunkley, J., et al., Seven-year Wilkinson Microwave Anisotropy Probe (WMAP) Observations: Cosmological Interpretation. 2011, ApJS, 192, 18, arXiv:1001.4538

Kovács, A. & Granett, B. R., Cold imprint of supervoids in the Cosmic Microwave Background re-considered with Planck and BOSS DR10. 2015, ArXiv e-prints, arXiv:1501.03376

Lewis, A. & Challinor, A., Weak gravitational lensing of the CMB. 2006,

Phys. Rep., 429, 1, arXiv:astro-ph/0601594
Lewis, A., Challinor, A., & Hanson, D., The shape of the CMB lensing bispectrum. 2011, J. Cosmology Astropart. Phys., 3, 18, arXiv:1101.2234
Li, H. & Xia, J., Constraints on dark energy parameters from correlations of CMB with LSS. 2010, J. Cosmology Astropart. Phys., 4, 26, arXiv:1004.2774
Mangilli, A. & Verde, L., Non-Gaussianity and the CMB bispectrum: Confusion between primordial and lensing-Rees-Sciama contribution? 2009, Phys. Rev. D, 80, 123007, arXiv:0906.2317
Manzotti, A. & Dodelson, S., Mapping the Integrated Sachs-Wolfe Effect. 2014, ArXiv e-prints, arXiv:1407.5623
Martinez-Gonzalez, E., Sanz, J. L., & Silk, J., Anisotropies in the microwave sky due to nonlinear structures. 1990, ApJ, 355, L5
McEwen, J. D., Vielva, P., Hobson, M. P., Martínez-González, E., & Lasenby, A. N., Detection of the integrated Sachs-Wolfe effect and corresponding dark energy constraints made with directional spherical wavelets. 2007, MNRAS, 376, 1211, arXiv:astro-ph/0602398
Neyrinck, M. C., ZOBOV: a parameter-free void-finding algorithm. 2008, MNRAS, 386, 2101, arXiv:0712.3049
Neyrinck, M. C., Gnedin, N. Y., & Hamilton, A. J. S., VOBOZ: an almost-parameter-free halo-finding algorithm. 2005, MNRAS, 356, 1222, arXiv:astro-ph/0402346
Nolta, M. R., Wright, E. L., Page, L., et al., First Year Wilkinson Microwave Anisotropy Probe Observations: Dark Energy Induced Correlation with Radio Sources. 2004, ApJ, 608, 10, arXiv:astro-ph/0305097
Okamoto, T. & Hu, W., Cosmic microwave background lensing reconstruction on the full sky. 2003, Phys. Rev. D, 67, 083002, arXiv:astro-ph/0301031
Padmanabhan, N., Hirata, C. M., Seljak, U., et al., Correlating the CMB with luminous red galaxies: The integrated Sachs-Wolfe effect. 2005, Phys. Rev. D, 72, 043525, arXiv:astro-ph/0410360
Pápai, P., Szapudi, I., & Granett, B. R., ISW Imprint of Superstructures on Linear Scales. 2010, ArXiv e-prints, arXiv:1012.3750
Pietrobon, D., Balbi, A., & Marinucci, D., Dark Energy Constraints from Needlets Analysis of Wmap3 and NVSS Data. 2006, arXiv:astro-ph/0611797, arXiv:astro-ph/0611797
Planck Collaboration ES. 2015, The Explanatory Supplement to the Planck 2015 results, http://wiki.cosmos.esa.int/planckpla/index.php/Main_Page (ESA)
Planck Collaboration XVII, *Planck* 2013 results. XVII. Gravitational lensing by large-scale structure. 2014, A&A, 571, A17, arXiv:1303.5077
Planck Collaboration XIX, *Planck* 2013 results. XIX. The integrated Sachs-Wolfe effect. 2014, A&A, 571, A19, arXiv:1303.5079
Planck Collaboration XXIV, *Planck* 2013 results. XXIV. Constraints on primordial non-Gaussianity. 2014, A&A, 571, A24, arXiv:1303.5084
Planck Collaboration I, *Planck* 2015 results. I. Overview of products and results. 2015, in preparation
Planck Collaboration II, *Planck* 2015 results. II. Low Frequency Instrument data processing. 2015, in preparation
Planck Collaboration III, *Planck* 2015 results. III. LFI systematic uncertainties. 2015, in preparation
Planck Collaboration IV, *Planck* 2015 results. IV. LFI beams and window functions. 2015, in preparation
Planck Collaboration V, *Planck* 2015 results. V. LFI calibration. 2015, in preparation
Planck Collaboration VI, *Planck* 2015 results. VI. LFI maps. 2015, in preparation
Planck Collaboration VII, *Planck* 2015 results. VII. High Frequency Instrument data processing: Time-ordered information and beam processing. 2015, in preparation
Planck Collaboration VIII, *Planck* 2015 results. VIII. High Frequency Instrument data processing: Calibration and maps. 2015, in preparation
Planck Collaboration IX, *Planck* 2015 results. IX. Diffuse component separation: CMB maps. 2015, in preparation
Planck Collaboration X, *Planck* 2015 results. X. Diffuse component separation: Foreground maps. 2015, in preparation
Planck Collaboration XI, *Planck* 2015 results. XI. CMB power spectra, likelihood, and consistency of cosmological parameters. 2015, in preparation
Planck Collaboration XII, *Planck* 2015 results. XII. Simulations. 2015, in preparation
Planck Collaboration XIII, *Planck* 2015 results. XIII. Cosmological parameters. 2015, in preparation
Planck Collaboration XIV, *Planck* 2015 results. XIV. Dark energy and modified gravity. 2015, in preparation
Planck Collaboration XV, *Planck* 2015 results. XV. Gravitational lensing. 2015, in preparation
Planck Collaboration XVI, *Planck* 2015 results. XVI. Isotropy and statistics of the CMB. 2015, in preparation
Planck Collaboration XVII, *Planck* 2015 results. XVII. Constraints on primordial non-Gaussianity. 2015, in preparation
Planck Collaboration XVIII, *Planck* 2015 results. XVIII. Background geometry and topology of the Universe. 2015, in preparation
Planck Collaboration XIX, *Planck* 2015 results. XIX. Constraints on primordial magnetic fields. 2015, in preparation
Planck Collaboration XX, *Planck* 2015 results. XX. Constraints on inflation. 2015, in preparation
Planck Collaboration XXI, *Planck* 2015 results. XXI. The integrated Sachs-Wolfe effect. 2015, in preparation
Planck Collaboration XXII, *Planck* 2015 results. XXII. A map of the thermal Sunyaev-Zeldovich effect. 2015, in preparation
Planck Collaboration XXIII, *Planck* 2015 results. XXIII. Thermal Sunyaev-Zeldovich effect–cosmic infrared background correlation. 2015, in preparation
Planck Collaboration XXIV, *Planck* 2015 results. XXIV. Cosmology from Sunyaev-Zeldovich cluster counts. 2015, in preparation
Planck Collaboration XXV, *Planck* 2015 results. XXV. Diffuse, low-frequency Galactic foregrounds. 2015, in preparation
Planck Collaboration XXVI, *Planck* 2015 results. XXVI. The Second Planck Catalogue of Compact Sources. 2015, in preparation
Planck Collaboration XXVII, *Planck* 2015 results. XXVII. The Second Planck Catalogue of Sunyaev-Zeldovich Sources. 2015, in preparation
Planck Collaboration XXVIII, *Planck* 2015 results. XXVIII. The Planck Catalogue of Cold Clumps. 2015, in preparation
Rassat, A., Land, K., Lahav, O., & Abdalla, F. B., Cross-correlation of 2MASS and WMAP 3: implications for the integrated Sachs-Wolfe effect. 2007, MNRAS, 377, 1085, arXiv:astro-ph/0610911
Rassat, A., Starck, J.-L., & Dupé, F.-X., Removal of two large-scale cosmic microwave background anomalies after subtraction of the integrated Sachs-Wolfe effect. 2013, A&A, 557, A32, arXiv:1303.4727
Rees, M. J. & Sciama, D. W., Larger scale Density Inhomogeneities in the Universe. 1968, Nature, 217, 511
Sachs, R. K. & Wolfe, A. M., Perturbations of a Cosmological Model and Angular Variations of the Microwave Background. 1967, ApJ, 147, 73
Savitzky, A. & Golay, M. J. E., Smoothing and differentiation of data by simplified least squares procedures. 1964, Analytical Chemistry, 36, 1627
Seljak, U. & Zaldarriaga, M., Direct signature of an evolving gravitational potential from the cosmic microwave background. 1999, Phys. Rev. D, 60, 043504, arXiv:astro-ph/9811123
Serra, P. & Cooray, A., Impact of secondary non-Gaussianities on the search for primordial non-Gaussianity with CMB maps. 2008, Phys. Rev. D, 77, 107305, arXiv:0801.3276
Sheth, R. K. & Tormen, G., Large-scale bias and the peak background split. 1999, MNRAS, 308, 119, arXiv:astro-ph/9901122
Smith, K. M. & Zaldarriaga, M., Algorithms for bispectra: forecasting, optimal analysis and simulation. 2011, MNRAS, 417, 2, arXiv:astro-ph/0612571
Sugiyama, N., Cosmic Background Anisotropies in Cold Dark Matter Cosmology. 1995, ApJS, 100, 281, arXiv:astro-ph/9412025
Verde, L. & Spergel, D. N., Dark energy and cosmic microwave background bispectrum. 2002, Phys. Rev. D, 65, 043007, arXiv:astro-ph/0108179
Vielva, P., Martínez-González, E., & Tucci, M., Cross-correlation of the cosmic microwave background and radio galaxies in real, harmonic and wavelet spaces: detection of the integrated Sachs-Wolfe effect and dark energy constraints. 2006, MNRAS, 365, 891, arXiv:astro-ph/0408252
Wright, E. L., Eisenhardt, P. R. M., Mainzer, A. K., et al., The Wide-field Infrared Survey Explorer (WISE): Mission Description and Initial On-orbit Performance. 2010, AJ, 140, 1868, arXiv:1008.0031
Xia, J.-Q., Baccigalupi, C., Matarrese, S., Verde, L., & Viel, M., Constraints on primordial non-Gaussianity from large scale structure probes. 2011, J. Cosmology Astropart. Phys., 8, 33, arXiv:1104.5015
Xia, J.-Q., Viel, M., Baccigalupi, C., & Matarrese, S., The high redshift Integrated Sachs-Wolfe effect. 2009, J. Cosmology Astropart. Phys., 9, 3, arXiv:0907.4753
Yan, L., Donoso, E., Tsai, C.-W., et al., Characterizing the Mid-infrared Extragalactic Sky with WISE and SDSS. 2013, AJ, 145, 55, arXiv:1209.2065
Zhao, G., Giannantonio, T., Pogosian, L., et al., Probing modifications of general relativity using current cosmological observations. 2010, Phys. Rev. D, 81, 103510, arXiv:1003.0001

[1] APC, AstroParticule et Cosmologie, Université Paris Diderot, CNRS/IN2P3, CEA/lrfu, Observatoire de Paris, Sorbonne Paris Cité, 10, rue Alice Domon et Léonie Duquet, 75205 Paris Cedex 13, France
[2] Aalto University Metsähovi Radio Observatory and Dept of Radio Science and Engineering, P.O. Box 13000, FI-00076 AALTO, Finland

[3] African Institute for Mathematical Sciences, 6-8 Melrose Road, Muizenberg, Cape Town, South Africa
[4] Agenzia Spaziale Italiana Science Data Center, Via del Politecnico snc, 00133, Roma, Italy
[5] Aix Marseille Université, CNRS, LAM (Laboratoire d'Astrophysique de Marseille) UMR 7326, 13388, Marseille, France
[6] Astrophysics Group, Cavendish Laboratory, University of Cambridge, J J Thomson Avenue, Cambridge CB3 0HE, U.K.
[7] Astrophysics & Cosmology Research Unit, School of Mathematics, Statistics & Computer Science, University of KwaZulu-Natal, Westville Campus, Private Bag X54001, Durban 4000, South Africa
[8] Atacama Large Millimeter/submillimeter Array, ALMA Santiago Central Offices, Alonso de Cordova 3107, Vitacura, Casilla 763 0355, Santiago, Chile
[9] CITA, University of Toronto, 60 St. George St., Toronto, ON M5S 3H8, Canada
[10] CNRS, IRAP, 9 Av. colonel Roche, BP 44346, F-31028 Toulouse cedex 4, France
[11] CRANN, Trinity College, Dublin, Ireland
[12] California Institute of Technology, Pasadena, California, U.S.A.
[13] Centre for Theoretical Cosmology, DAMTP, University of Cambridge, Wilberforce Road, Cambridge CB3 0WA, U.K.
[14] Centro de Estudios de Física del Cosmos de Aragón (CEFCA), Plaza San Juan, 1, planta 2, E-44001, Teruel, Spain
[15] Computational Cosmology Center, Lawrence Berkeley National Laboratory, Berkeley, California, U.S.A.
[16] Consejo Superior de Investigaciones Científicas (CSIC), Madrid, Spain
[17] DSM/Irfu/SPP, CEA-Saclay, F-91191 Gif-sur-Yvette Cedex, France
[18] DTU Space, National Space Institute, Technical University of Denmark, Elektrovej 327, DK-2800 Kgs. Lyngby, Denmark
[19] Département de Physique Théorique, Université de Genève, 24, Quai E. Ansermet,1211 Genève 4, Switzerland
[20] Departamento de Física, Universidad de Oviedo, Avda. Calvo Sotelo s/n, Oviedo, Spain
[21] Department of Astronomy and Astrophysics, University of Toronto, 50 Saint George Street, Toronto, Ontario, Canada
[22] Department of Astrophysics/IMAPP, Radboud University Nijmegen, P.O. Box 9010, 6500 GL Nijmegen, The Netherlands
[23] Department of Physics & Astronomy, University of British Columbia, 6224 Agricultural Road, Vancouver, British Columbia, Canada
[24] Department of Physics and Astronomy, Dana and David Dornsife College of Letter, Arts and Sciences, University of Southern California, Los Angeles, CA 90089, U.S.A.
[25] Department of Physics and Astronomy, University College London, London WC1E 6BT, U.K.
[26] Department of Physics, Florida State University, Keen Physics Building, 77 Chieftan Way, Tallahassee, Florida, U.S.A.
[27] Department of Physics, Gustaf Hällströmin katu 2a, University of Helsinki, Helsinki, Finland
[28] Department of Physics, Princeton University, Princeton, New Jersey, U.S.A.
[29] Department of Physics, University of California, Santa Barbara, California, U.S.A.
[30] Department of Physics, University of Illinois at Urbana-Champaign, 1110 West Green Street, Urbana, Illinois, U.S.A.
[31] Dipartimento di Fisica e Astronomia G. Galilei, Università degli Studi di Padova, via Marzolo 8, 35131 Padova, Italy
[32] Dipartimento di Fisica e Scienze della Terra, Università di Ferrara, Via Saragat 1, 44122 Ferrara, Italy
[33] Dipartimento di Fisica, Università La Sapienza, P. le A. Moro 2, Roma, Italy
[34] Dipartimento di Fisica, Università degli Studi di Milano, Via Celoria, 16, Milano, Italy
[35] Dipartimento di Fisica, Università degli Studi di Trieste, via A. Valerio 2, Trieste, Italy
[36] Dipartimento di Fisica, Università di Roma Tor Vergata, Via della Ricerca Scientifica, 1, Roma, Italy
[37] Dipartimento di Matematica, Università di Roma Tor Vergata, Via della Ricerca Scientifica, 1, Roma, Italy
[38] Discovery Center, Niels Bohr Institute, Blegdamsvej 17, Copenhagen, Denmark
[39] Dpto. Astrofísica, Universidad de La Laguna (ULL), E-38206 La Laguna, Tenerife, Spain
[40] European Southern Observatory, ESO Vitacura, Alonso de Cordova 3107, Vitacura, Casilla 19001, Santiago, Chile
[41] European Space Agency, ESAC, Planck Science Office, Camino bajo del Castillo, s/n, Urbanización Villafranca del Castillo, Villanueva de la Cañada, Madrid, Spain
[42] European Space Agency, ESTEC, Keplerlaan 1, 2201 AZ Noordwijk, The Netherlands
[43] Facoltà di Ingegneria, Università degli Studi e-Campus, Via Isimbardi 10, Novedrate (CO), 22060, Italy
[44] Gran Sasso Science Institute, INFN, viale F. Crispi 7, 67100 L'Aquila, Italy
[45] HGSFP and University of Heidelberg, Theoretical Physics Department, Philosophenweg 16, 69120, Heidelberg, Germany
[46] Helsinki Institute of Physics, Gustaf Hällströmin katu 2, University of Helsinki, Helsinki, Finland
[47] INAF - Osservatorio Astronomico di Padova, Vicolo dell'Osservatorio 5, Padova, Italy
[48] INAF - Osservatorio Astronomico di Roma, via di Frascati 33, Monte Porzio Catone, Italy
[49] INAF - Osservatorio Astronomico di Trieste, Via G.B. Tiepolo 11, Trieste, Italy
[50] INAF/IASF Bologna, Via Gobetti 101, Bologna, Italy
[51] INAF/IASF Milano, Via E. Bassini 15, Milano, Italy
[52] INFN, Sezione di Bologna, Via Irnerio 46, I-40126, Bologna, Italy
[53] INFN, Sezione di Roma 1, Università di Roma Sapienza, Piazzale Aldo Moro 2, 00185, Roma, Italy
[54] INFN, Sezione di Roma 2, Università di Roma Tor Vergata, Via della Ricerca Scientifica, 1, Roma, Italy
[55] INFN/National Institute for Nuclear Physics, Via Valerio 2, I-34127 Trieste, Italy
[56] IPAG: Institut de Planétologie et d'Astrophysique de Grenoble, Université Grenoble Alpes, IPAG, F-38000 Grenoble, France, CNRS, IPAG, F-38000 Grenoble, France
[57] IUCAA, Post Bag 4, Ganeshkhind, Pune University Campus, Pune 411 007, India
[58] Imperial College London, Astrophysics group, Blackett Laboratory, Prince Consort Road, London, SW7 2AZ, U.K.
[59] Infrared Processing and Analysis Center, California Institute of Technology, Pasadena, CA 91125, U.S.A.
[60] Institut Néel, CNRS, Université Joseph Fourier Grenoble I, 25 rue des Martyrs, Grenoble, France
[61] Institut Universitaire de France, 103, bd Saint-Michel, 75005, Paris, France
[62] Institut d'Astrophysique Spatiale, CNRS (UMR8617) Université Paris-Sud 11, Bâtiment 121, Orsay, France
[63] Institut d'Astrophysique de Paris, CNRS (UMR7095), 98 bis Boulevard Arago, F-75014, Paris, France
[64] Institute for Space Sciences, Bucharest-Magurale, Romania
[65] Institute of Astronomy, University of Cambridge, Madingley Road, Cambridge CB3 0HA, U.K.
[66] Institute of Theoretical Astrophysics, University of Oslo, Blindern, Oslo, Norway
[67] Instituto de Astrofísica de Canarias, C/Vía Láctea s/n, La Laguna, Tenerife, Spain
[68] Instituto de Física de Cantabria (CSIC-Universidad de Cantabria), Avda. de los Castros s/n, Santander, Spain
[69] Istituto Nazionale di Fisica Nucleare, Sezione di Padova, via Marzolo 8, I-35131 Padova, Italy
[70] Jet Propulsion Laboratory, California Institute of Technology, 4800 Oak Grove Drive, Pasadena, California, U.S.A.

[71] Jodrell Bank Centre for Astrophysics, Alan Turing Building, School of Physics and Astronomy, The University of Manchester, Oxford Road, Manchester, M13 9PL, U.K.
[72] Kavli Institute for Cosmology Cambridge, Madingley Road, Cambridge, CB3 0HA, U.K.
[73] LAL, Université Paris-Sud, CNRS/IN2P3, Orsay, France
[74] LAPTh, Univ. de Savoie, CNRS, B.P.110, Annecy-le-Vieux F-74941, France
[75] LERMA, CNRS, Observatoire de Paris, 61 Avenue de l'Observatoire, Paris, France
[76] Laboratoire AIM, IRFU/Service d'Astrophysique - CEA/DSM - CNRS - Université Paris Diderot, Bât. 709, CEA-Saclay, F-91191 Gif-sur-Yvette Cedex, France
[77] Laboratoire Traitement et Communication de l'Information, CNRS (UMR 5141) and Télécom ParisTech, 46 rue Barrault F-75634 Paris Cedex 13, France
[78] Laboratoire de Physique Subatomique et Cosmologie, Université Grenoble-Alpes, CNRS/IN2P3, 53, rue des Martyrs, 38026 Grenoble Cedex, France
[79] Laboratoire de Physique Théorique, Université Paris-Sud 11 & CNRS, Bâtiment 210, 91405 Orsay, France
[80] Lawrence Berkeley National Laboratory, Berkeley, California, U.S.A.
[81] Lebedev Physical Institute of the Russian Academy of Sciences, Astro Space Centre, 84/32 Profsoyuznaya st., Moscow, GSP-7, 117997, Russia
[82] Max-Planck-Institut für Astrophysik, Karl-Schwarzschild-Str. 1, 85741 Garching, Germany
[83] McGill Physics, Ernest Rutherford Physics Building, McGill University, 3600 rue University, Montréal, QC, H3A 2T8, Canada
[84] National University of Ireland, Department of Experimental Physics, Maynooth, Co. Kildare, Ireland
[85] Niels Bohr Institute, Blegdamsvej 17, Copenhagen, Denmark
[86] Optical Science Laboratory, University College London, Gower Street, London, U.K.
[87] SB-ITP-LPPC, EPFL, CH-1015, Lausanne, Switzerland
[88] SISSA, Astrophysics Sector, via Bonomea 265, 34136, Trieste, Italy
[89] School of Physics and Astronomy, Cardiff University, Queens Buildings, The Parade, Cardiff, CF24 3AA, U.K.
[90] School of Physics and Astronomy, University of Nottingham, Nottingham NG7 2RD, U.K.
[91] Sorbonne Université-UPMC, UMR7095, Institut d'Astrophysique de Paris, 98 bis Boulevard Arago, F-75014, Paris, France
[92] Space Research Institute (IKI), Russian Academy of Sciences, Profsoyuznaya Str, 84/32, Moscow, 117997, Russia
[93] Space Sciences Laboratory, University of California, Berkeley, California, U.S.A.
[94] Special Astrophysical Observatory, Russian Academy of Sciences, Nizhnij Arkhyz, Zelenchukskiy region, Karachai-Cherkessian Republic, 369167, Russia
[95] Stanford University, Dept of Physics, Varian Physics Bldg, 382 Via Pueblo Mall, Stanford, California, U.S.A.
[96] Sub-Department of Astrophysics, University of Oxford, Keble Road, Oxford OX1 3RH, U.K.
[97] Theory Division, PH-TH, CERN, CH-1211, Geneva 23, Switzerland
[98] UPMC Univ Paris 06, UMR7095, 98 bis Boulevard Arago, F-75014, Paris, France
[99] Universität Heidelberg, Institut für Theoretische Astrophysik, Philosophenweg 12, 69120 Heidelberg, Germany
[100] Université de Toulouse, UPS-OMP, IRAP, F-31028 Toulouse cedex 4, France
[101] Universities Space Research Association, Stratospheric Observatory for Infrared Astronomy, MS 232-11, Moffett Field, CA 94035, U.S.A.
[102] University of Granada, Departamento de Física Teórica y del Cosmos, Facultad de Ciencias, Granada, Spain
[103] University of Granada, Instituto Carlos I de Física Teórica y Computacional, Granada, Spain
[104] Warsaw University Observatory, Aleje Ujazdowskie 4, 00-478 Warszawa, Poland